Silicone Wire Embolization-induced Acute Retinal Artery Ischemia and Reperfusion Model in Mouse: Gene Expression Provides Insight into Pathological Processes

Yuedan Wang[a#], Ying Li[a#], Jiaqing Feng[a#], Chuansen Wang[a], Yuwei Wan[a], Bingyang Lv[a], Yinming Li[b], Hao Xie[b], Ting Chen[a], Faxi Wang[b], Ziyue Li[a], Anhuai Yang[a*] & Xuan Xiao[a,b*]

a Department of Ophthalmology, Renmin Hospital of Wuhan University, Wuhan 430060, Hubei, China

b Department of Clinical Laboratory, Institute of Translational Medicine, Renmin Hospital of Wuhan University, Wuhan 430060, Hubei, China

# These authors contributed equally.

*** Correspondence to:** Xuan Xiao, Department of Ophthalmology, Renmin Hospital of Wuhan University, No. 238 Jie Fang Road, Wuhan 430060, Hubei, China. Tel: (86) 027-88041911, Email: xiaoxuan1111@whu.edu.cn

*** Correspondence to:** Anhuai Yang, Department of Ophthalmology, Renmin Hospital of Wuhan University, No. 238 Jie Fang Road, Wuhan 430060, Hubei, China. Email: yah0525@126.com

Abstract

Acute retinal ischemia and ischemia-reperfusion injury are the primary causes of retinal neural cell death and vision loss in retinal artery occlusion (RAO). The absence of an accurate mouse model for simulating the retinal ischemic process has hindered progress in developing neuroprotective agents for RAO. We developed a unilateral pterygopalatine ophthalmic artery occlusion (UPOAO) mouse model using silicone wire embolization combined with carotid artery ligation. The survival of retinal ganglion cells and visual function were evaluated to determine the duration of ischemia. Immunofluorescence staining, optical coherence tomography, and haematoxylin and eosin staining were utilized to assess changes in major neural cell classes and retinal structure degeneration at two reperfusion durations. Transcriptomics was employed to investigate alterations in the pathological process of UPOAO following ischemia and reperfusion, highlighting transcriptomic differences between UPOAO and other retinal ischemia-reperfusion models. The UPOAO model successfully replicated the acute interruption of retinal blood supply observed in RAO. 60-minutes of Ischemia led to significant loss of major retinal neural cells and visual function impairment. Notable thinning of the inner retinal layer, especially the ganglion cell layer, was evident post-UPOAO. Temporal transcriptome analysis revealed various pathophysiological processes related to immune cell migration, oxidative stress, and immune inflammation during the non-reperfusion and reperfusion periods. A pronounced increase in microglia within the retina and peripheral leukocytes accessing the retina was observed during reperfusion periods. Comparison of differentially expressed genes (DEGs) between the UPOAO and high intraocular

pressure models revealed specific enrichments in lipid and steroid metabolism-related genes in the UPOAO model. The UPOAO model emerges as a novel tool for screening pathogenic genes and promoting further therapeutic research in RAO.

Key words: Retinal artery occlusion; Mouse model; Ischemia and reperfusion injury; Transcriptomics; Immune cell

1 Introduction

Retinal artery occlusion (RAO) is a severe ophthalmic disease characterized by a sudden interruption of blood flow in the retinal artery, leading to retinal ischemia [1]. Over 60% of RAO patients suffer from impaired vision, ranging from finger counting to complete vision loss [2]. Additionally, RAO patients face increased risk of cardiovascular and cerebrovascular events [3-5]. Retinal ischemia and hypoxia can lead to irreversible damage to retinal cells within 90 minutes [6]. This damage is primarily due to the apoptosis of retinal ganglion cells (RGCs), which is driven by inflammation and oxidative stress. Unfortunately, conservative treatments for RAO, such as ocular massage and hyperbaric oxygen therapy, provide limited therapeutic benefits [7]. Although thrombolysis is effective, its application is restricted by a narrow therapeutic window (typically within 4.5 hours) [8]. Furthermore, the restoration of blood flow to the ischemic area following thrombolysis can cause a sudden increase in tissue oxidative levels, resulting in ischemia-reperfusion injury (IRI) in the retina [9]. IRI is a common pathological condition that can induce inflammation, retinal tissue damage and visual impairment [10]. Therefore, it is crucial to develop an animal model that accurately

67 simulates the pathological processes of RAO to thoroughly investigate the
68 pathophysiological changes and explore potential neuroprotective treatments following
69 retinal ischemia and reperfusion.
70
71 Various animal models have been employed to investigate the effects of retinal injury
72 resulting from ischemia and subsequent reperfusion in RAO [6, 11, 12]. Based on the
73 methods used for modelling, retinal ischemia-reperfusion models can be categorized into
74 two groups: 1) intravascular occlusion models, including photochemical-induced
75 thrombosis model and vascular intervention model; and 2) extravascular occlusion
76 models, including central retinal artery ligation (CRAL) model, unilateral common carotid
77 artery occlusion (UCCAO) model, and high intraocular pressure (HIOP) model. The
78 photochemical-induced thrombosis model and vascular intervention model have been
79 reported to be useful tools for assessing retinal injury after ischemia and reperfusion.
80 However, both models are limited by the need for trained interventional radiologists and
81 the need for advanced techniques [13, 14]. The CRAL model, which directly clips or
82 ligates the central retinal artery, also presents drawbacks, such as potential optic nerve
83 damage and difficulty in application to small animals such as mice, limiting its use in
84 experiments with larger sample sizes [6]. The UCCAO model, which induces retinal
85 hypoperfusion by occluding the unilateral common carotid artery (CCA), is more suitable
86 for simulating chronic ischemic retinal disease than acute retinal ischemia [15, 16]. The
87 HIOP model is widely utilized in mice for studying ischemia-reperfusion in acute primary
88 angle-closure glaucoma (APACG) [17]. However, the mechanical compression of the

89 retina caused by saline injection in this model may also lead to retinal damage,
90 potentially influencing IRI research. Therefore, it is critically important to develop a simple
91 and low-skill-required mouse model that can simulate acute retinal ischemia and
92 reperfusion injury in RAO patients.
93
94 To better simulate the retinal ischemic process and possible IRI following RAO, we
95 developed a novel vascular-associated mouse model called the unilateral pterygopalatine
96 ophthalmic artery occlusion (UPOAO) model. In this model, we employed silicone wire
97 embolization and carotid artery ligation to completely block the blood supply to the retina.
98 We characterized the major classes of retinal neural cells and evaluated visual function
99 following different durations of ischemia (30 minutes and 60 minutes) and reperfusion (3-
100 days and 7-days) after UPOAO. Additionally, we utilized transcriptomics to investigate
101 the transcriptional changes and elucidate the pathophysiological process of the UPOAO
102 model after ischemia and reperfusion. Finally, we highlighted the transcriptomic
103 differences between this model and other retinal ischemia-reperfusion models, including
104 HIOP and UCCAO, revealing the unique pathological processes that closely resemble
105 retinal IRI in RAO. The UPOAO model offers new insights into the mechanisms and
106 pathways involved in ischemia and reperfusion studies of RAO, providing a foundation for
107 studying protective strategies for ocular ischemic diseases.
108
109 **2 Methods and materials**
110 2.1 Animals

111 Eight-week-old male C57BL/6 mice were used in the experiments. Only male mice were
112 used to exclude the potential influence of oestrogenic hormones. The mice were provided
113 sufficient food and water and were maintained on a 12-hour dark-light cycle in a room
114 with regulated temperature conditions. All the experimental procedures were designed
115 and conducted according to the ethical guidelines outlined in the Association for
116 Research in Vision and Ophthalmology (ARVO) Statement for the Use of Animals in
117 Ophthalmic and Vision Research. The study protocol and methods received approval
118 from the Experimental Animal Ethics Committee of Renmin Hospital of Wuhan University
119 (approval number: WDRM-20220305A).
120
121 2.2 Preparation and surgical procedure of the UPOAO model
122 Eight-week-old male C57BL/6 mice weighing 20-25 grams were used in this study. An
123 isoflurane-based anaesthesia system was used to induce and maintain general
124 anaesthesia in the mice during surgical procedures. The mice were anaesthetized with a
125 1.5-2% concentration of isoflurane delivered in a mixture of nitrous oxide and oxygen via
126 rubber tubing. Body temperature was maintained at 37 ± 0.5°C throughout the surgery.
127 Surgical instruments were sterilized with 75% ethanol before use to ensure sterility.
128
129 We drew inspiration from the widely employed middle cerebral artery occlusion (MCAO)
130 model [18, 19], commonly used in cerebral ischemic injury research, which guided the
131 development of the UPOAO model. The mouse was gently positioned in a supine posture
132 on a heating blanket, and its neck was exposed. The preparation involved depilation of

133 the neck area, followed by skin disinfection, and finally, a midline incision along the neck
134 was made. After separating the neck gland using two tweezers, careful blunt dissection
135 was employed to separate the left CCA, internal carotid artery (ICA) and external carotid
136 artery (ECA), avoiding the compression of nearby nerves and veins (**Fig. 1A**) (**Video 1**).
137 Then, the CCA and ICA were ligated with a 6-0 suture. A knot was secured using a 6-0
138 suture at the distal end of the ECA, and a slipknot was created at the proximal end (**Fig.**
139 **1B**). To preserve the reperfusion process and avoid bleeding and mortality during surgery,
140 a silicone wire embolus was inserted through the ECA instead of through the CCA.
141 Ophthalmic scissors were used to make a small inverted "V"-shaped incision between
142 the two suture knots on the ECA. A specialized silicone wire embolus, measuring 7 ± 0.1
143 mm in length and 0.21 ± 0.1 mm in diameter, was inserted through the incision, directing
144 it into the ECA and further into the CCA (**Fig. 1C**). Next, the ligation on the ICA was
145 removed, and the ECA was cut at the point where the artery had been previously incised
146 with scissors. Subsequently, the silicone wire embolus was retracted to the bifurcation of
147 the CCA, rotated counterclockwise, and inserted into the ICA and further into the
148 pterygopalatine artery (PPA) (**Fig. 1D1**). The silicone tail of the silicone wire embolus was
149 positioned near the bifurcation of the CCA (**Fig. 1D2**), effectively obstructing the
150 ophthalmic artery (OA) (**Video 2**). Then, the slipknot was fastened, and the skin was
151 sutured. The mouse was free to move around during arterial embolization.
152
153 Following a predetermined ischemia embolization time, the silicone wire embolus was
154 carefully removed from the PPA without massive haemorrhage (**Fig. 1E**). The CCA

155 suture was removed, restoring arterial reperfusion (**Fig. 1F**) (**Video 3**). Then, the skin
156 wound was sutured, and the mice were routinely fed during reperfusion (**Fig. 1G**).
157
158 2.3 Staining of retinal vessels
159 To clearly visualize the retinal vessels, rhodamine-labelled canavalin A was used for
160 mouse heart perfusion. Each mouse was anaesthetized with 1% sodium pentobarbital
161 and placed in the supine position on a foam board resting on a tray. The sternum was
162 opened to expose the heart. A needle attached to the perfusion tube was inserted into
163 the left ventricle via the apex of the mouse heart and secured. The right atrial appendage
164 was dissected with scissors to allow blood outflow. Saline solution was perfused through
165 the left ventricle using a pump system to drain blood from the arteries. Subsequently, the
166 prepared solution of rhodamine-labelled canavalin A was injected into the mice and
167 circulated throughout the mouse vessels for 30 minutes. The mice were then sacrificed,
168 and their eyes were removed and immersed in paraformaldehyde (PFA) for one hour in
169 the dark. A flat-mounted retina was obtained, and retinal images were captured using a
170 Leica SP8 confocal microscope equipped with a 10× objective.
171
172 2.4 Quantification of RGCs and microglia
173 The mice were euthanized by cervical dislocation, and their eyes were fixed in 4% PFA
174 for 60 minutes at room temperature (RT). Subsequently, the cornea and lens were
175 excised, and the intact retina was isolated for retinal flat mounting. The retina was
176 immersed in PBS supplemented with 5% bovine serum albumin (BSA) and 0.5% Triton

177 X-100 for overnight blocking and then incubated with Brn3a antibody (Synaptic Systems,
178 Germany) or Iba1 antibody (Wako, Japan). Following a two-day incubation with the
179 primary antibody, the retina was gently washed three times with PBS. Subsequently, the
180 retina was incubated with Alexa Fluor 594 (AntGene, Wuhan, China) in a light-protected
181 cassette for two days. After three rinses, the retina was uniformly sectioned into a four-
182 leaf clover morphology and flattened using a coverslip. Retinal flat mounts labelled with
183 Brn3a were photographed to count using a fluorescence microscope (BX51, Olympus,
184 Japan) and representative pictures were imaged using a Leica SP8 confocal microscope
185 (Leica TCS SP8, Germany). Retinas labelled with Iba1 were imaged utilizing a
186 fluorescence microscope (BX63; Olympus, Tokyo, Japan). Each quadrant of the retina
187 was systematically subdivided into central, middle, and peripheral fields (distance from
188 the optic nerve head: central field: 0.1 mm to 0.5 mm, middle field: 0.9 mm to 1.3 mm,
189 and peripheral field: 1.7 mm to 2.1 mm). The surviving RGCs and activated microglia of
190 12 fields in each retina were quantified and averaged using ImageJ software (National
191 Institutes of Health, USA).
192
193 2.5 Electroretinogram (ERG)
194 Mice were dark-adapted overnight before ERG, and all subsequent procedures were
195 carried out in the dark. Before ERG, the mice were anaesthetized with 1% sodium
196 pentobarbital via intraperitoneal injection, and their pupils were dilated. A subcutaneous
197 electrode was inserted into the posterior cervical skin, a tail electrode was affixed to the
198 posterior end of the mouse tail, and the corneal electrode was gently placed on the

199 central corneal surface. A RetiMINER-C visual electrophysiological system (3VMED Co.,
200 Ltd., Shanghai, China) was used for recording electrical responses. The a-waves, b-
201 waves, and oscillatory potentials (OPs) after flash stimuli of 0.01, 0.03, 0.1, 0.3, 1.0, 3.0,
202 and 10.0 cd.s/m^2 in scotopic adaptation were recorded. The amplitudes and implicit times
203 of a-waves, b-waves, and OPs in response to various flash stimuli were analysed.
204
205 2.6 Optical Coherence Tomography Imaging (OCT) and Fluorescein Fundus
206 Angiography (FFA)
207 The mice were placed on the platform of a Spectralis HRA + OCT device (Heidelberg
208 Engineering, Heidelberg, Germany) for OCT imaging following anaesthesia. Pupil dilation
209 was performed, and normal saline was applied regularly to maintain corneal moisture.
210 The focal length of the device was adjusted until the mouse retina was clearly visible.
211 The head of the mouse was gently repositioned to capture images of the peripheral
212 fundus. The multiline mode was used to scan each layer of the retina, and four quadrants
213 of view centred on the nipple in the upper left, lower left, upper right, and lower right were
214 recorded. In this study, the total retinal thickness was manually segmented into three
215 parts and encompassed the entire thickness from the nerve fibre layer to the
216 photoreceptor layer. The ganglion cell complex (GCC) was defined as the combined
217 thickness of the retinal nerve fibre layer (RNFL), ganglion cell layer (GCL), and inner
218 plexiform layer (IPL). The inner nuclear layer (INL) and the outer plexiform layer (OPL)
219 were combined for thickness analysis due to the difficulty in distinguishing between these
220 layers. The remaining retinal layers, including the outer nuclear layer (ONL), inner

221 segment/outer segment (IS/OS), and retinal pigment epithelium (RPE) layers, were
222 measured together. The thickness of the retina at 1.5 papillary diameters (PD), 3.0 PD,
223 and 4.5 PD from the centre of the optic disc was measured using the Heidelberg
224 measuring tool.
225
226 For FFA, the mice were anaesthetized, and their pupils were dilated. Subsequently,
227 fundus angiography was performed immediately following an intraperitoneal injection of
228 sodium fluorescein. Images were acquired alternately for both eyes within 5 seconds of
229 the injection.
230
231 2.7 Hematoxylin and eosin (HE)
232 Mouse eyes were fixed in FAS eyeball fixation solution (Service-bio, Wuhan, China) for
233 48 hours, followed by dehydration and subsequent embedding in paraffin. The paraffin
234 blocks were trimmed parallel to the optic nerve to obtain 3-4 μm thick sections where the
235 optic nerve was located. Six paraffin sections from each eyeball were stained with HE.
236 Images were captured using an Olympus fluorescence microscope. The retinal thickness
237 within a range of 200-1100 μm from the optic disc was measured using Image-Pro Plus
238 6.0 software.
239
240 2.8 Staining of Retinal Sections
241 For immunofluorescence, mouse eyes were fixed in 4% PFA solution and subjected to
242 gradient dehydration using 10%, 20%, and 30% sucrose solutions. The following day, the

243 eyes were embedded in optimum cutting temperature (OCT) compound (SAKURA, USA)
244 and frozen at -80°C. Several 14-μm-thick frozen sections were obtained from each
245 eyeball through the use of a freezing microtome (Leica, Wetzlar, Germany). The section
246 surface was parallel to the optic nerve, and 3-6 frozen sections were mounted on a single
247 slide. The slides were stored at -20°C until use.
248
249 All sections were blocked with 5% BSA and 0.5% Triton X-100 in PBS for 2 hours.
250 Primary antibodies, as listed in **Table 1**, were diluted in PBS containing 5% BSA and 0.5%
251 Triton X-100 and incubated at 4°C overnight. The following day, after three rinses, the
252 sections were incubated with secondary antibodies at RT for 2 hours in a cassette,
253 followed by three washes. The sections were then stained with DAPI (Service-bio,
254 Wuhan, China) for 15 minutes. After the final three rinses, the frozen sections were
255 sealed. A Leica SP8 instrument equipped with a 40× objective was used to photograph
256 frozen sections near the optic nerve head. The fluorescence intensity of all slices of each
257 eye was determined using ImageJ software.
258
259 2.9 Surgical procedure for the UCCAO model and the HIOP model
260 Animals for the UCCAO model were prepared and managed according to the procedure
261 described for the UPOAO model. After blunt dissection, the left CCA was ligated with a 6-
262 0 suture. After 60 minutes of ligation, the suture was removed, and the skin wound was
263 subsequently closed with sutures. Mice were routinely fed during the reperfusion period,
264 and the retinas of UCCAO mice were harvested 7-days post-surgery.

265

266 The HIOP model was generated based on previously established methods [20]. Briefly,
267 mice were anaesthetized by intraperitoneal injection of 1% sodium pentobarbital. Pupils
268 were dilated using tropicamide phenylephrine eye drops (0.5% tropicamide and 0.5%
269 deoxyadrenaline hydrochloride, Santen Pharmaceutical) applied 5 minutes in advance.
270 An insulin hypodermic needle attached to a silicone elastomer tube was inserted into the
271 anterior chamber of the unilateral experimental eye. The IOP was elevated for 60
272 minutes by raising the height of the saline solution storage bag to 162 cm, after which the
273 needle was removed to immediately restore the IOP to baseline levels. Iris whitening and
274 loss of retinal red-light reflexes indicated retinal ischemia. After surgery, levofloxacin
275 hydrochloride ophthalmic gel was applied to the eyes of the mice. Retinas from HIOP
276 mice were collected 7-days post-surgery.

277

278 2.10 Transcriptome sequence and analysis

279 Retinal samples from UPOAO, HIOP, and UCCAO mice were extracted and promptly
280 frozen in liquid nitrogen within 10 minutes of cervical dislocation. Total RNA extraction
281 was performed according to the protocol outlined in the TRIzol Reagent manual (Life
282 Technologies, CA, USA). RNA integrity and concentration were assessed using an
283 Agilent 2,100 Bioanalyzer (Agilent Technologies, Inc., Santa Clara, CA, USA). The
284 resulting RNA samples were then pooled and subjected to sequencing on the Illumina
285 HiSeq3000 platform in a 150-bp paired-end read format. The raw RNA-sequencing
286 (RNA-seq) reads were preprocessed and quantified using the featureCounts function in

287 the SubReads package version 1.5.3, with default parameters.

288

289 RNA-seq analysis was conducted on samples from 5 mice in the non-perfusion group, 4
290 mice in the 3-days perfusion group, and 5 mice in the 7-days perfusion group of the
291 UPOAO model. Additionally, retinas from both the 7-days HIOP experimental eyes and
292 bilateral UCCAO eyes were collected (n=5) for analysis.

293

294 Data normalization and subsequent processing utilized the 'limma' package in R software
295 (version 4.2.3) [21]. Volcano plots and Venn diagrams were generated for visualization to
296 identify significantly differentially expressed genes (DEGs) and perform Gene Ontology
297 (GO) annotation analysis. DEGs with a |log2-fold change (FC)| > 1 and adjusted p value
298 < 0.05 were significantly differentially expressed. Enrichment analysis focused on DEGs
299 with an adjusted p < 0.05 and an enriched gene count > 5. To visualize the expression
300 patterns of significant DEGs, a heatmap was generated using the 'pheatmap' package.
301 Gene Set Enrichment Analysis (GSEA) was conducted using the GSEA program (version
302 4.3.2) [22], employing the default gene set m-subset (mh.all.v2023.1.mm.symbols.gmt) to
303 explore significant functional and pathway differences. Enriched pathways were classified
304 based on criteria such as adjusted p value (< 0.05), false discovery rate (FDR) q value (<
305 0.25), and normalized enrichment score (|NES| > 1). Furthermore, protein–protein
306 interaction (PPI) analysis was performed using the Search Tool for the Retrieval of
307 Interacting Genes (STRING) database (https://string-db.org/) [23]. Genes with a greater
308 degree of protein-level interactions with others were further analysed using Cytoscape

309 software (version 3.8.2) to generate a downstream PPI map. PPI pairings with an
310 interaction score > 0.7 were extracted and visualized using Cytoscape 3.9.0 [24].
311
312 2.11 Real-time Quantitative polymerase chain reaction (RT-qPCR)
313 RNA was extracted from fresh mouse retinal samples and subjected to reverse
314 transcription using HiScript III RT SuperMix for qPCR (Vazyme, China) following the
315 manufacturer's instructions. RT–qPCR analysis was conducted on a CFX instrument
316 (Bio-Rad) using AceQ qPCR SYBR Green Master Mix (Vazyme, China). The PCR
317 program comprised 40 cycles of 10 seconds at 95°C and 30 seconds at 60°C. Assays
318 were performed in triplicate, and Ct values were normalized to beta-actin levels. Relative
319 quantification of target gene expression was calculated using the 2-ΔΔCt method. The
320 primer sequences are provided in **Table S1**.
321
322 2.12 Statistical Analysis
323 All the data were analysed using GraphPad Prism version 9.0 (GraphPad Software, San
324 Diego, CA, USA). Each experimental group included a minimum of three biological
325 replicates. T tests, including RGCs and microglia counting, OPs analysis, retinal
326 thickness measurements via HE staining, and fluorescence intensity quantification, were
327 used to compare the two groups. Two-way ANOVA (two-way analysis of variance) test
328 was used for more than two different experimental groups, including ERG waves and
329 retinal thickness measurements in OCT. All data are presented as the mean ± standard
330 error of the mean (SEM), and the statistical graphs are shown as scatter bar graphs and

331 line charts. $P < 0.05$ was considered to indicate statistical significance.

332

333 **3 Results**

334 3.1 Silicone wire embolus insertion interrupts retinal blood flow

335 To reproduce the retinal ischemic process and potential IRI in RAO, we established a
336 mouse model of UPOAO by combining silicone wire embolization with carotid artery
337 ligation. Model validation was conducted through a series of experiments, with detailed
338 descriptions provided in the Materials and Methods section (**Fig. 1A-G**). To confirm blood
339 flow disruption, we performed cardiac perfusion with fluorescently labelled lectin and FFA.
340 Rhodamine-labelled canavalin A was used during in vivo perfusion with silicone wire
341 embolus, and both eyes were evaluated. The sham eye exhibited normal blood perfusion
342 in the retina, while the experimental eye showed no perfusion (**Fig. 1H, I**). FFA revealed
343 delayed and limited perfusion in the experimental lateral retina, primarily near the optic
344 disc (**Fig. 1J, K**). These findings indicate that the insertion of the silicone wire embolus
345 effectively impaired blood flow to the retina.

346

347 3.2 60-minute ischemia in UPOAO damage retinal structure and function

348 To investigate the optimal ischemic duration, the mice were subjected to ischemic
349 periods of 30 and 60 minutes, followed by reperfusion periods of 3-days and 7-days.
350 Retinal structure and visual function were assessed through flat-mounted retina analysis
351 and flash ERG.

352

353 In the 30-minute ischemia group, no significant RGCs death was observed after 3-days
354 (**Fig. 2A, B**) or 7-days of reperfusion (**Fig. 2C, D**). However, after 60 minutes of ischemia
355 followed by either 3-days or 7-days of reperfusion, reductions in RGCs density were
356 evident (**Fig. 2E-H**). ERG results showed no statistical difference in amplitudes between
357 bilateral eyes after 3- and 7-days of 30-minutes reperfusion (**Fig. 3A-C**). However, the b-
358 wave amplitude notably decreased after 60 minutes of ischemia and 3-days of
359 reperfusion (**Fig. 3D**). By 7-days of reperfusion, the b-wave amplitude had halved
360 compared to that of the sham eyes (**Fig. 3E**). The appearance times of the a-waves and
361 b-waves in the experimental and control eyes remained consistent across all four groups
362 (**Fig. S1**). Additionally, OPs have also been used to sensitively monitor retinal ischemic
363 effects by detecting changes before any alterations in b-waves occur [25-27]. The
364 amplitudes of OPs in the experimental eyes, particularly in the 60-minute ischemia and 7-
365 days reperfusion group, significantly decreased to less than 50% of those in the sham
366 eyes (**Fig. 3F, G**). Based on RGCs survival and changes in ERG waves, we determined
367 that a 60-minute ischemic duration is optimal for the UPOAO model.
368
369 3.3 Evaluation of retinal thickness in UPOAO through OCT and HE
370 To assess retinal thickness non-invasively in the UPOAO model, we conducted OCT
371 imaging during 3-days and 7-days reperfusion periods. Following a 3-days reperfusion
372 period, no significant changes were observed in the GCC, INL + OPL, and ONL + IS/OS
373 + RPE layers at 1.5, 3, and 4.5 PD from the optic disc (**Fig. 4B, Fig. S2A, B**). However,
374 the total retinal thickness decreased at 4.5 PD (**Fig. 4C**). After 7-days of reperfusion, the

375 total retinal thickness decreased at 1.5 PD, 3 PD, and 4.5 PD, primarily due to inner
376 retinal thinning (**Fig. 4D-F, Fig. S2C, D**).
377
378 For a detailed analysis of inner retinal thickness, we extracted UPOAO mouse eyes and
379 stained them with HE. The thickness of the RNFL + GCL increased at 3-days of
380 reperfusion (**Fig. 4H**), followed by a decrease at 7-days of reperfusion (**Fig. 4L**). IPL
381 thickness decreased at both 3-days and 7-days of reperfusion (**Fig. 4I, M**), while INL
382 thickness decreased only at 7-days of reperfusion (**Fig. 4N**). We hypothesized that the
383 initial swelling of the GCL in response to acute ischemia and hypoxia led to early
384 thickening, followed by gradual thinning due to tissue dysfunction. This hypothesis was
385 supported by the observation of RGCs loss and reduced GCC thickness evaluated by
386 OCT at 7-days (**Fig. 4E**).
387
388 We observed by OCT that changes in retinal thickness became noticeable at 3-days
389 post-UPOAO and exhibited a significant decrease at 7-days. HE results further revealed
390 that alterations in inner retinal thickness constituted a substantial portion of the total
391 retinal thickness during the early reperfusion stage after UPOAO.
392
393 3.4 Survival of retinal neural cells in UPOAO
394 Given that mouse retinal function heavily relies on rod cells and that scotopic (low light)
395 vision is primarily governed by rod photoreceptors, the observed reductions in b-wave
396 and OPs-wave amplitudes indicate impaired synaptic transmission within the inner retina

397 [28]. Our OCT and HE findings suggested structural injuries within the inner retina.
398 Notably, the thickness of the outer retinal layers in OCT remained unchanged. To further
399 explore these observations, we conducted immunofluorescence staining to investigate
400 alterations in major retinal cell types, primarily focusing on bipolar cells (BCs),
401 photoreceptor cells, horizontal cells (HCs), and cholinergic amacrine cells.
402
403 3.4.1 BCs loss and photoreceptor cells survival
404 PKCα serves as a marker delineating BCs, with their cell bodies primarily located in the
405 outermost part of the INL, axonal terminals extending into the innermost part of the IPL,
406 and dendrites confined to the OPL (**Fig. 5A, B**). In the experimental UPOAO eyes, BCs
407 did not show significant changes at the 3-days reperfusion mark but exhibited dramatic
408 alterations by the 7-days reperfusion period (**Fig. 5A2, B2**). In particular, the
409 immunostaining density of BCs dendritic and axonal arbors notably decreased at the 7-
410 days reperfusion mark. BCs account for approximately 40% of INL cells in mice, and their
411 somata and axonal processes form a substantial part of the INL and IPL, consistent with
412 the thinning of the INL observed in both OCT and HE at 7-days (**Fig. 4E, N**). Notably, the
413 decrease in the number of PKCα^{+} BCs at the 7-days reperfusion point coincided with the
414 decrease in the b-waves amplitude in ERG (**Fig. 3E**), indicating functional interplay
415 between BCs and other cells.
416
417 Recoverin marks the somata and outer segments of photoreceptor cells and is localized
418 within the ONL (**Fig. S3A, B**). Interestingly, recoverin-positive photoreceptors remained

419 relatively stable throughout the reperfusion periods, which aligns with the unchanged
420 thickness of the outer retinal layers observed in OCT (**Fig. S2C, D**).
421
422 3.4.2 HCs and cholinergic amacrine cells loss
423 We evaluated HCs and cholinergic amacrine cells using calbindin and ChAT
424 immunostaining, respectively. Calbindin immunostaining highlighted the somata of HCs
425 within the INL, with terminal axon connections linearly positioned within the OPL (**Fig. 5E,**
426 **F**). In the UPOAO experimental eyes, no significant change in the number of HCs was
427 observed during the 3-days reperfusion period, while a notable reduction was observed
428 after 7 days. By 7-days, a significant decrease in cell body numbers, a considerable
429 reduction in axon density, and disrupted linear connections were observed (**Fig. 5F2**).
430
431 ChAT$^+$ cell bodies were located in the GCL and INL, with dendrites forming two narrow
432 stratified bands within the IPL. The immunofluorescence density of ChAT$^+$ amacrine cells
433 decreased notably after 3 days and even more prominently after 7 days (**Fig. 5I, J**). The
434 fluorescence intensity of the two bands within the IPL markedly decreased and was
435 nearly invisible after 7 days (**Fig. 5J2**).
436
437 3.5 Time course transcriptome analysis revealed features of different reperfusion periods
438 in UPOAO
439 To explore the pathophysiological processes of UPOAO, we extracted retinas from both
440 eyes for transcriptome sequencing. The samples included retinas from eyes subjected to

441 60 minutes of ischemia without reperfusion, 60 minutes of ischemia followed by 3-days of
442 reperfusion, and 60 minutes of ischemia followed by 7-days of reperfusion, with the
443 sham-treated eyes serving as controls.
444
445 In the non-perfusion group, 215 genes were upregulated and 204 genes were
446 downregulated (**Fig. 6A**). GO enrichment analysis revealed that the DEGs were related to
447 leukocyte migration, epidermis development, myeloid leukocyte migration and other cell
448 migration pathways (**Fig. 6B**). The heatmap and box showed the upregulated and
449 downregulated genes involved in immune cell migration-related pathways during the non-
450 perfusion period in UPOAO (**Fig. 6C**). High-connectivity DEGs ('hub genes'), such as
451 Dusp1 and Fos, were also enriched in these pathways (**Fig. S4A**). GSEA also showed
452 similar results (**Fig. S4B-D**). These results suggested that in the early stage of retinal
453 ischemic injury, leukocytes from the microvasculature may infiltrate retinal tissue. More
454 experimental validation will be performed to confirm this hypothesis.
455
456 In the 3-days reperfusion group, 372 genes were upregulated, and 170 genes were
457 downregulated (**Fig. 6D**). GO enrichment analysis revealed that the DEGs at 3-days after
458 reperfusion were related to energy metabolism, mitochondrial regulation, and oxidative
459 stress pathways (**Fig. 6E**). The heatmap and box displayed the upregulated and
460 downregulated genes involved in oxidative stress-related pathways at the 3-days
461 reperfusion stage in UPOAO, including hub genes such as Mrpl18 and Mrps23 (**Fig. 6F,**
462 **Fig. S5A**). GSEA revealed changes in pathways related to the binding membrane of

463 organelles, the cell surface and the plasma membrane protein complex (**Fig. S5B**).
464 Furthermore, 44 overlapping genes between the mitochondrial genes and DEGs at 3-
465 days post-UPOAO were mainly related to mitochondrial transport and the mitochondrial
466 tricarboxylic acid cycle (**Fig. S5C, D**). These results suggested that mitochondria and
467 metabolism play significant roles in IRI.
468
469 In the 7-days reperfusion group, 429 genes were upregulated, and 310 genes were
470 downregulated (**Fig 6G**). The DEGs at this stage were enriched in pathways related to
471 immune effector processes, positive regulation of responses to external stimuli and
472 inflammation (**Fig. 6H**). A heatmap was generated to show the upregulated and
473 downregulated genes of immune inflammation-related pathways at 7-days after
474 reperfusion in UPOAO, and most hub genes, such as Cd86, Cd48, Tlr4, and Tlr6 were
475 also enriched in these pathways (**Fig. 6I, Fig. S6A**). GSEA also showed similar results
476 (**Fig S6B**). Moreover, RT–qPCR confirmed the upregulation of immune inflammation-
477 related gene expression (**Fig. S7**). Significantly, 112 genes that overlapped between
478 immune-related genes and DEGs at 7-days post-UPOAO were primarily associated with
479 immune receptor activity and phagocytic vesicles (**Fig. S6C, D**). These results
480 underscore the predominant role of immune responses during this stage.
481
482 To explore the associations between changes observed at 3-days and 7-days after
483 reperfusion, we analyzed the DEGs and identified 17 overlapping genes (**Fig. S8A**),
484 which were mainly associated with the nitric oxide biosynthetic process (**Fig. S8B**). Our

485 findings suggest that the immune inflammatory response observed after 7-days of
486 reperfusion may represent the cumulative effect of the acute oxidative stress response
487 during the initial 3-days reperfusion period.
488
489 3.6 Leukocyte Infiltration and Microglial Activation
490 Time course transcriptome analysis underscored the predominant role of immune
491 inflammatory responses during the reperfusion stage. Previous reports have indicated
492 that the inflammatory response in retinal ischemia-reperfusion injury (RIRI) is
493 orchestrated by peripheral immune cells and resident immune cells within the retina [29,
494 30]. In our study, we demonstrated the presence of leukocyte infiltration and microglial
495 activation in the UPOAO model. Immunofluorescence staining for CD45 was performed
496 on retinas at different time points post modelling to visualize the distribution and quantity
497 of white blood cells (**Fig. 7A-D**). Laser confocal Z-plane projections confirmed minimal
498 leukocyte infiltration in the retinas of sham eyes, which showed that $CD45^+$ cells in the
499 vascular lumen likely represented patrolling cells (**Fig. 7A**). A significant increase in
500 $CD45^+$ cells was observed in UPOAO model retinas after 1 day (**Fig. 7E**), with a
501 progressive increase in quantity over time (**Fig. 7F, G**). Notably, the majority of $CD45^+$
502 cells in UPOAO model retinas at 1-day displayed a morphology similar to that of vascular
503 leukocytes (**Fig. 7B**), suggesting a large influx of peripheral white blood cells into the
504 retinal tissue. In contrast, $CD45^+$ cells at 3-days and 7-days of reperfusion exhibited a
505 combination of amoeboid and branched morphologies (**Fig. 7C, D**), indicative of activated
506 states.

507

508 Microglia, which are known to undergo activation and morphological changes in response
509 to various insults, were examined in the superficial retinas of sham and UPOAO eyes.
510 Immunofluorescence staining for Iba1 was conducted on flat-mounted retinas at 3-days
511 and 7-days post-reperfusion. In sham eyes, Iba1^{+} microglia displayed small somas and
512 elongated dendrites that were evenly distributed within the retina (**Fig. 7H1, I1**).
513 Conversely, UPOAO retinas exhibited numerous activated Iba1^{+} microglia with enlarged
514 somas, shortened dendrites, and an ameboid appearance (**Fig. 7H2, I2**). The number of
515 Iba1^{+} microglia in UPOAO retinas was approximately five times greater than that in sham
516 eyes at 3-days (**Fig. 7J**), with a further increase observed at 7-days (**Fig. 7K**), although
517 this increase was less pronounced than that at the 3-days time point (**Fig. 7J**). These
518 results indicated a potential reduction in immune-mediated inflammation over time.

519

520 3.7 RNA-seq comparison between UPOAO and extravascular occlusion models

521 To further study the characteristics of UPOAO, we analyzed the transcriptomes of two
522 extravascular occlusion models: HIOP and UCCAO. The HIOP model induces ischemia
523 through anterior chamber perfusion with normal saline (**Fig. 8A**), while the UCCAO model
524 involves ligation of the unilateral common carotid artery (**Fig. 8H**). RNA-seq analysis of
525 retinas subjected to 60 minutes of ischemia followed by 7-days of reperfusion in the
526 HIOP model revealed enrichment of immune-related pathways, specifically highlighting
527 increased activity in leukocyte-mediated immunity and regulation of immune effector
528 processes (**Fig. 8B**). This finding was consistent with the results of GO analysis, which

529 revealed associations of the overlapping DEGs between the HIOP and UPOAO models
530 with toll-like receptor binding, T-cell receptor binding, and immune-related functions (**Fig.**
531 **8C, D**). To further explore these DEGs, we explored the remaining DEGs in the HIOP
532 model in addition to the overlapping genes. GO analysis revealed that the remaining
533 DEGs in the HIOP model were also enriched in immune responses, such as the T-cell
534 receptor complex pathway, adaptive immune response, and B-cell-mediated immunity
535 function (**Fig. 8E**). Remarkably, upon examining the remaining DEGs specific to the
536 UPOAO model, GO analysis revealed DEGs distinctly related to lipid and steroid
537 metabolic processes (**Fig. 8F, G**). This observation indicates that the UPOAO model,
538 which is closely related to RAO, involves not only conventional immune responses but
539 also unique regulation of lipid and steroid metabolism.
540
541 Similarly, the UCCAO model exhibited associations with negative regulation of B-cell
542 proliferation, lymphocyte activation, and related processes (**Fig. 8I**). Additionally, the hub
543 genes identified through protein–protein interaction (PPI) analysis are presented (**Fig. 8J**).
544 However, the UCCAO model displayed minimal overlap with the UPOAO model, with
545 only 15 overlapping DEGs identified in the Venn diagram analysis (**Fig. 8K**). Further
546 analysis of the UCCAO DEGs revealed two genes (Mettl14 and YTHDF2) related to m6A
547 modifications (**Fig. 8L**). Although arterial blood flow is occluded in both the UPOAO and
548 UCCAO models, our results revealed that the pathophysiological processes of the two
549 models were particularly different after 7-days of reperfusion.
550

551 **4 Discussion**

552 This study aimed to develop a more appropriate mouse model for investigating the
553 ischemia-reperfusion process in RAO and unravelling the underlying pathophysiological
554 mechanisms. We combined silicone wire embolization with carotid artery ligation to
555 effectively block the blood supply to the retinal artery, closely mimicking the
556 characteristics of the acute interruption of blood supply in RAO patients [31]. In the
557 UPOAO model, a 60-minute ischemia period was sufficient to simulate the injury of major
558 retinal neural cells, such as RGCs, BCs, HCs, and cholinergic amacrine cells, resulting in
559 visual impairment. Moreover, histologic examination demonstrated thinning of the inner
560 layer of the retina, especially the GCL. Time course transcriptome analysis revealed
561 various pathophysiological processes related to immune cell migration, oxidative stress,
562 and immune inflammation during non-reperfusion and reperfusion periods. The resident
563 microglia within the retina and peripheral leukocytes that access the retina were markedly
564 increased during reperfusion periods. Additionally, we compared the transcriptomic
565 signatures of the UPOAO model with those of two commonly used ischemia-reperfusion
566 mouse models (HIOP and UCCAO), highlighting the potential relevance of the UPOAO
567 model to ocular vascular occlusive diseases.

568

569 The UPOAO mouse model effectively simulates the characteristic features of RAO
570 observed in patients. RAO patients often exhibit distinctive patterns in dark-adapted
571 ERGs, where b-waves are reduced while a-waves remain stable [32-34]. In our study, we
572 observed almost the same phenomenon in ERG amplitude after 60 minutes of ischemia

573 in the UPOAO model (Table S2). This observation was further confirmed by
574 immunofluorescence staining of bipolar cells and photoreceptor cells. Importantly, a
575 previous study linked the thinning of the inner retina with alterations in ERG in patients
576 with RAO [35]. Our results showed that ischemic damage predominantly affected the
577 inner retinal layers, while the outer layer was almost unaffected (**Table S2**). This
578 distinction is attributed to the reliance of the inner layers on the retinal artery for blood
579 supply, whereas the outer layers are supplied by the choroid. Additionally, histological
580 examination revealed increased retinal NFL and GCL thickness and decreased IPL
581 thickness after 3-days of reperfusion, indicating that ischemia-induced oedema had not
582 completely subsided.
583
584 This study comprehensively explored the transcriptomic signature after ischemia and
585 revealed that resident and peripheral immune cells may play major roles in pathological
586 processes. In the non-reperfusion group, the transcriptional changes were primarily
587 involved in the migration of immune cells such as leukocytes and neutrophils from blood
588 vessels into ischemic retinal tissue. This process is closely linked to injury during
589 ischemia and reperfusion, where leukocytes and neutrophils infiltrate neural tissue
590 through the vascular endothelium [36, 37]. Our results revealed an increase in $CD45^+$
591 leukocytes in the retina and retinal microvasculature, suggesting that these leukocytes
592 were recruited from the bloodstream to the damaged retinal tissue following reperfusion.
593 During leukocyte access to the retina, chemokines, chemokine receptors, adhesion
594 molecules and cytoskeletal components play important roles in regulating endothelial

595 permeability and facilitating leukocyte adhesion to endothelial cells [38, 39]. Our findings
596 of related gene expression are consistent with this mechanism.
597
598 During the 3-days reperfusion period, we observed that an increased number of DEGs
599 were significantly involved in the critical pathological response to oxidative stress in the
600 context of IR tissues. The generation of reactive oxygen species (ROS) in mitochondria
601 and subsequent oxidative stress are widely recognized as major causes of retinal cell
602 damage induced by IR [40, 41]. This finding suggested that mitochondrial function, which
603 is involved in oxidative stress processes, may play an important role in the
604 pathophysiology of IRI during the early reperfusion stage. Oxidative stress can influence
605 the permeability of the inner blood retina barrier (iBRB), allowing leukocytes to access
606 retinal tissues [42]. The infiltration and activation of immune cells are recognized as the
607 underlying causes of many retinal diseases, including ischemic ophthalmia [42, 43]. In
608 the UPOAO model, the increase in $CD45^+$ leukocytes and $Iba1^+$ microglia in the retina
609 after 3-days of reperfusion supports this viewpoint.
610
611 In the later stage of reperfusion (7-days), the DEGs were mainly enriched in immune
612 regulation and inflammation. With more upregulated DEGs than downregulated ones, we
613 hypothesize that the activation of the immune inflammatory response contributes to
614 further IRI in retinal tissue. Previous studies have shown that the retina can elicit
615 immunological responses during ischemia-reperfusion injury and that immune
616 inflammation is an important phenomenon in the progression of this injury [30]. The

617 excessive ROS generated by mitochondria in RGCs during the activation of inflammatory
618 responses can damage cell structure and visual function [44]. Microglia, considered the
619 primary resident immune cells, contribute to inflammatory responses and consequent
620 neural damage [45]. Infiltrating leukocytes can activate resident microglia, forming a
621 feedback loop that exacerbates inflammation [46]. Complex interactions between
622 immune cells and retinal neurons after RIRI have been reported [47]. Interestingly, in our
623 UPOAO model, the death of major retinal neural cells, such as RGCs, BCs, and HCs,
624 was correlated with an increase in infiltrating leukocytes and resident microglia.
625 Therefore, we considered that the immune response and neuroinflammation observed
626 after 7-days of reperfusion may result from the cumulative effects of acute oxidative
627 stress and the responses of resident and peripheral immune cells (**Fig. 9, Table S2**). In
628 summary, we described the pathological processes at different time points and
629 highlighted the important role of resident and peripheral immune cell responses in the
630 UPOAO model. This finding offers valuable insights for subsequent screening of
631 pathogenic genes and potential immunotherapy approaches.
632
633 Compared with the HIOP and UCCAO models, the UPOAO model is a more appropriate
634 choice for studying retinal IRI in RAO. The HIOP model, widely used for investigating the
635 pathogenesis of APACG, exhibits retinal degeneration features similar to those of the
636 UPOAO model during both reperfusion periods [48]. In our UPOAO model, histologic and
637 immunohistochemical analysis demonstrated that 60 minutes of ischemia followed by 3-
638 days or 7-days of reperfusion can cause irreversible damage to retinal structure and

639 visual function. Specifically, we observed distinct alterations, such as thinning of the inner
640 retina, substantial RGCs apoptosis, and decreased b-wave amplitude. Multiple studies on
641 the HIOP model have reported consistent results [45, 49, 50]. However, some typical
642 phenotypes in the HIOP model, such as thinning of the outer nuclear layer and the entire
643 neuroretina and decreased a-wave amplitude, were not observed in the UPOAO model.
644 Moreover, our transcriptome sequencing revealed a specific subset of DEGs unique to
645 the UPOAO model, including Apoe, Abca1, Ldlr, Cyp39a1, and Bmp6. Notably, these
646 DEGs were significantly enriched in pathways associated with lipid and steroid synthesis.
647 Steroid and lipid metabolism homeostasis is disrupted under conditions of oxidative
648 stress and inflammation [51]. In the UPOAO model, the observed lipid and steroid
649 biological processes may result from the cumulative pathological responses triggered by
650 IRI, as observed in the HIOP model. In the UCCAO model, RNA-seq revealed that DEGs
651 were enriched in two main pathways: 1) epigenetic modification-related pathways,
652 including nucleobase-containing compound catabolic process, RNA catabolic process,
653 mRNA catabolic process and N6-methyladenosine (m6A) modification; and 2) cell death
654 pathways, including regulation of autophagosome assembly, negative regulation of
655 neuron death, and negative regulation of the neuronal apoptotic process. Epigenetic
656 mechanisms may play a key role in the pathophysiology of ocular disease [52]. m6A, one
657 of the most common RNA modifications, has been reported to regulate cell death
658 processes, including apoptosis and autophagy, in the pathological process of IRI [53].
659 These results suggest that epigenetic mechanisms may significantly influence cell death
660 during the 7-days reperfusion period in the UCCAO model. Lee et al. evaluated the

661 characteristics of UCCAO without reperfusion using visual, histological and
662 immunohistochemical approaches. Their results revealed delayed perfusion of the
663 ipsilateral retina, thinning of the inner retinal layer 10 weeks after surgery, and a dramatic
664 decrease in the amplitudes of b-waves on day 14 after UCCAO [15, 54]. This finding
665 suggested that UCCAO primarily represents a model of retinal hypoperfusion injury and
666 may not effectively reflect acute ischemic-induced structural and functional damage in
667 RAO (**Fig. 9**). These results led us to consider the UPOAO model an effective
668 experimental model for studying the pathological processes underlying acute ischemia
669 and IRI.
670
671 Our research has certain limitations that should be acknowledged. First, our study
672 focused on the changes that occurred within 60 minutes of ischemia and within the first
673 7-days of reperfusion in the UPOAO model. Further exploration is needed to understand
674 the changes induced by longer reperfusion periods. Additionally, we proposed possible
675 pathological mechanisms, including iBRB damage, oxidative stress and immune
676 inflammation, mainly based on the enrichment results of DEGs at three reperfusion time
677 points. More molecular experimental validation is required to substantiate these proposed
678 mechanisms.
679
680 In summary, by thoroughly exploring the injury to major retinal neural cells, visual
681 impairment and pathophysiological changes in the UPOAO model, we confirmed that this
682 model can effectively simulate the acute ischemia-reperfusion processes in RAO. It

683 serves as an ideal mouse model for investigating the underlying pathological
684 mechanisms of ischemia and reperfusion. Furthermore, our UPOAO model holds great
685 promise as a novel model for studies on pathogenic genes and potential therapeutic
686 interventions for RAO.
687

688 **Acknowledgements**

689 The authors would like to express their gratitude to all participants involved in the
690 experiments. The authors also wish to acknowledge the Eye Institute of Renmin Hospital
691 of Wuhan University for providing us with the experimental facilities and environment.
692 Special thanks are extended to Professor Shenqi Zhang for the technical support in the
693 surgical procedure of UPOAO model.
694

695 **Availability of data and materials**

696 All data are available from the corresponding author upon reasonable request.
697

698 **Authors' contributions**

699 Xiao X and Yang AH conceived the project and supervised, guided the research. Li Y,
700 Wang YD and Feng JQ wrote the draft, Feng JQ, Wang CS, Xie H and Li ZY revised the
701 manuscript. Wang YD and Li Y constructed the animal models and obtained the data.
702 Wang YD performed the immunofluorescence staining, HE staining. Li Y and Feng JQ
703 performed the ERG, analyzed the RNA-seq data, and created the visualizations. Wan
704 YW and Wang YD performed the FFA and OCT imaging and Wan YW analyzed the data.

Lv BY and Wang YD took pictures and videos of the UPOAO model, and Feng JQ made schematic diagrams of modeling. Li YM, Xie H, Chen T, Wang FX provided support for the technical methods and contributed to the discussion, and reviewed the manuscript. All authors critically contributed to the manuscript, and have read and approved the final manuscript.

Funding

This work was supported by the National Nature Science Foundation of China (grant number: 82371079), National Key R&D Program of China (2023YFC2308404), Fundamental Research Funds for the Central Universities (2042023gf0013), Key research and development project of Hubei Province (grant number: 2022BCA009).

Ethics approval and consent to participate

All animal experiments were performed following the ethical guidelines outlined in the ARVO Statement for the Use of Animals in Ophthalmic and Vision Research, with the approval of the Experimental Animal Ethics Committee of Renmin Hospital of Wuhan University (approval number: WDRM-20220305A).

References

1. Scott, I.U., et al., *Retinal vascular occlusions.* Lancet, 2020. **396**(10266): p. 1927-1940.

727 2. Hayreh, S.S. and M.B. Zimmerman, *Central retinal artery occlusion: visual outcome.*
728 Am J Ophthalmol, 2005. **140**(3): p. 376-91.
729 3. Vestergaard, N., et al., *Risk of Stroke, Myocardial Infarction, and Death Among*
730 *Patients With Retinal Artery Occlusion and the Effect of Antithrombotic Treatment.*
731 Transl Vis Sci Technol, 2021. **10**(11): p. 2.
732 4. Fallico, M., et al., *Risk of acute stroke in patients with retinal artery occlusion: a*
733 *systematic review and meta-analysis.* Eye (Lond), 2020. **34**(4): p. 683-689.
734 5. Chen, T., et al., *Sex differences in major adverse cardiovascular and cerebrovascular*
735 *event risk among central retinal artery occlusion patients.* Sci Rep, 2023. **13**(1): p.
736 14930.
737 6. Prasad, S.S., et al., *Retinal gene expression after central retinal artery ligation:*
738 *effects of ischemia and reperfusion.* Invest Ophthalmol Vis Sci, 2010. **51**(12): p. 6207-
739 19.
740 7. Mac Grory, B., et al., *Management of Central Retinal Artery Occlusion: A Scientific*
741 *Statement From the American Heart Association.* Stroke, 2021. **52**(6): p. e282-e294.
742 8. Raber, F.P., et al., *Thrombolysis in central retinal artery occlusion: a retrospective*
743 *observational study.* J Neurol, 2023. **270**(2): p. 891-897.
744 9. Hu, H., et al., *Efficacy of Intra-Arterial Thrombolysis for Acute Central Retinal Artery*
745 *Occlusion: A Meta-Analysis.* Eur Neurol, 2022. **85**(3): p. 186-194.
746 10. Wan, P., et al., *LncRNA H19 initiates microglial pyroptosis and neuronal death in*
747 *retinal ischemia/reperfusion injury.* Cell Death Differ, 2020. **27**(1): p. 176-191.

748 11. Shabanzadeh, A.P., et al., *Neurosurgical Modeling of Retinal Ischemia-Reperfusion*
749 *Injury.* J Stroke Cerebrovasc Dis, 2018. **27**(4): p. 845-856.
750 12. Gao, Y., et al., *Novel Acute Retinal Artery Ischemia and Reperfusion Model in*
751 *Nonhuman Primates.* Stroke, 2020. **51**(8): p. 2568-2572.
752 13. Morén, H., et al., *The porcine retinal vasculature accessed using an endovascular*
753 *approach: a new experimental model for retinal ischemia.* Invest Ophthalmol Vis Sci,
754 2009. **50**(11): p. 5504-10.
755 14. Zhang, Y., et al., *Activation of the mitochondrial apoptotic pathway in a rat model of*
756 *central retinal artery occlusion.* Invest Ophthalmol Vis Sci, 2005. **46**(6): p. 2133-9.
757 15. Lee, D., et al., *A mouse model of retinal hypoperfusion injury induced by unilateral*
758 *common carotid artery occlusion.* Exp Eye Res, 2020. **201**: p. 108275.
759 16. Lee, D., et al., *Nicotinamide Mononucleotide Protects against Retinal Dysfunction in a*
760 *Murine Model of Carotid Artery Occlusion.* Int J Mol Sci, 2022. **23**(23).
761 17. van Zyl, T., et al., *Cell atlas of aqueous humor outflow pathways in eyes of humans*
762 *and four model species provides insight into glaucoma pathogenesis.* Proc Natl Acad
763 Sci U S A, 2020. **117**(19): p. 10339-10349.
764 18. Chiang, T., R.O. Messing, and W.H. Chou, *Mouse model of middle cerebral artery*
765 *occlusion.* J Vis Exp, 2011(48).
766 19. Sasaki, M., O. Honmou, and J.D. Kocsis, *A rat middle cerebral artery occlusion model*
767 *and intravenous cellular delivery.* Methods Mol Biol, 2009. **549**: p. 187-95.

768 20. Chen, Y.G., et al., *Increased nuclear factor-kappa B p65 immunoreactivity following*
769 *retinal ischemia and reperfusion injury in mice.* J Neurosci Res, 2003. **72**(1): p. 125-
770 31.
771 21. Ritchie, M.E., et al., *limma powers differential expression analyses for RNA-*
772 *sequencing and microarray studies.* Nucleic Acids Res, 2015. **43**(7): p. e47.
773 22. Subramanian, A., et al., *Gene set enrichment analysis: a knowledge-based approach*
774 *for interpreting genome-wide expression profiles.* Proc Natl Acad Sci U S A, 2005.
775 **102**(43): p. 15545-50.
776 23. Szklarczyk, D., et al., *STRING v11: protein-protein association networks with*
777 *increased coverage, supporting functional discovery in genome-wide experimental*
778 *datasets.* Nucleic Acids Res, 2019. **47**(D1): p. D607-d613.
779 24. Kohl, M., S. Wiese, and B. Warscheid, *Cytoscape: software for visualization and*
780 *analysis of biological networks.* Methods Mol Biol, 2011. **696**: p. 291-303.
781 25. Cao, W., et al., *Dextromethorphan attenuates the effects of ischemia on rabbit*
782 *electroretinographic oscillatory potentials.* Documenta Ophthalmologica, 1993. **84**(3):
783 p. 247-256.
784 26. Xu, J., et al., *Pregabalin Mediates Retinal Ganglion Cell Survival From Retinal*
785 *Ischemia/Reperfusion Injury Via the Akt/GSK3β/β-Catenin Signaling Pathway.* Invest
786 Ophthalmol Vis Sci, 2022. **63**(12): p. 7.
787 27. Takács, B., et al., *Electroretinographical Analysis of the Effect of BGP-15 in Eyedrops*
788 *for Compensating Global Ischemia-Reperfusion in the Eyes of Sprague Dawley Rats.*
789 Biomedicines, 2024. **12**(3).

790 28. Yang, Y., et al., *Tmem30a deficiency leads to retinal rod bipolar cell degeneration.* J
791 Neurochem, 2019. **148**(3): p. 400-412.
792 29. Li, G., et al., *Diagnostic and Immunosuppressive Potential of Elevated Mir-424 Levels*
793 *in Circulating Immune Cells of Ischemic Stroke Patients.* Aging Dis, 2018. **9**(2): p.
794 172-181.
795 30. Minhas, G., J. Sharma, and N. Khan, *Cellular Stress Response and Immune*
796 *Signaling in Retinal Ischemia-Reperfusion Injury.* Front Immunol, 2016. **7**: p. 444.
797 31. Biousse, V., F. Nahab, and N.J. Newman, *Management of Acute Retinal Ischemia:*
798 *Follow the Guidelines!* Ophthalmology, 2018. **125**(10): p. 1597-1607.
799 32. Block, F. and M. Schwarz, *The b-wave of the electroretinogram as an index of retinal*
800 *ischemia.* Gen Pharmacol, 1998. **30**(3): p. 281-7.
801 33. Lima, L.H., et al., *Unilateral electronegative ERG in a presumed central retinal artery*
802 *occlusion.* Clin Ophthalmol, 2010. **4**: p. 1311-4.
803 34. Suzuki, R., et al., *Degeneration and dysfunction of retinal neurons in acute ocular*
804 *hypertensive rats: involvement of calpains.* J Ocul Pharmacol Ther, 2014. **30**(5): p.
805 419-28.
806 35. Shinoda, K., et al., *Changes in retinal thickness are correlated with alterations of*
807 *electroretinogram in eyes with central retinal artery occlusion.* Graefes Arch Clin Exp
808 Ophthalmol, 2008. **246**(7): p. 949-54.
809 36. Szabo, M.E., et al., *Ischemia and reperfusion-induced histologic changes in the rat*
810 *retina. Demonstration of a free radical-mediated mechanism.* Invest Ophthalmol Vis
811 Sci, 1991. **32**(5): p. 1471-8.

812 37. Szabo, M.E., et al., *Ischaemia- and reperfusion-induced Na+, K+, Ca2+ and Mg2+*
813 *shifts in rat retina: effects of two free radical scavengers, SOD and EGB 761.* Exp
814 Eye Res, 1992. **55**(1): p. 39-45.
815 38. Johnson-Léger, C., M. Aurrand-Lions, and B.A. Imhof, *The parting of the endothelium:*
816 *miracle, or simply a junctional affair?* J Cell Sci, 2000. **113 (Pt 6)**: p. 921-33.
817 39. Springer, T.A., *Traffic signals for lymphocyte recirculation and leukocyte emigration:*
818 *the multistep paradigm.* Cell, 1994. **76**(2): p. 301-14.
819 40. Fang, I.M., C.M. Yang, and C.H. Yang, *Chitosan oligosaccharides prevented retinal*
820 *ischemia and reperfusion injury via reduced oxidative stress and inflammation in rats.*
821 Exp Eye Res, 2015. **130**: p. 38-50.
822 41. Oharazawa, H., et al., *Protection of the retina by rapid diffusion of hydrogen:*
823 *administration of hydrogen-loaded eye drops in retinal ischemia-reperfusion injury.*
824 Invest Ophthalmol Vis Sci, 2010. **51**(1): p. 487-92.
825 42. Kaur, C., W.S. Foulds, and E.A. Ling, *Blood-retinal barrier in hypoxic ischaemic*
826 *conditions: basic concepts, clinical features and management.* Prog Retin Eye Res,
827 2008. **27**(6): p. 622-47.
828 43. Eltzschig, H.K. and C.D. Collard, *Vascular ischaemia and reperfusion injury.* Br Med
829 Bull, 2004. **70**: p. 71-86.
830 44. Sanderson, T.H., et al., *Molecular mechanisms of ischemia-reperfusion injury in brain:*
831 *pivotal role of the mitochondrial membrane potential in reactive oxygen species*
832 *generation.* Mol Neurobiol, 2013. **47**(1): p. 9-23.

833 45. Abcouwer, S.F., et al., *Inflammatory resolution and vascular barrier restoration after*
834 *retinal ischemia reperfusion injury.* J Neuroinflammation, 2021. **18**(1): p. 186.
835 46. Au, N.P.B. and C.H.E. Ma, *Neuroinflammation, Microglia and Implications for Retinal*
836 *Ganglion Cell Survival and Axon Regeneration in Traumatic Optic Neuropathy.* Front
837 Immunol, 2022. **13**: p. 860070.
838 47. Qin, Q., et al., *Inhibiting multiple forms of cell death optimizes ganglion cells survival*
839 *after retinal ischemia reperfusion injury.* Cell Death Dis, 2022. **13**(5): p. 507.
840 48. Yao, F., et al., *Pathologically high intraocular pressure disturbs normal iron*
841 *homeostasis and leads to retinal ganglion cell ferroptosis in glaucoma.* Cell Death
842 Differ, 2023. **30**(1): p. 69-81.
843 49. Zeng, Z., et al., *Pathologically high intraocular pressure induces mitochondrial*
844 *dysfunction through Drp1 and leads to retinal ganglion cell PANoptosis in glaucoma.*
845 Redox Biol, 2023. **62**: p. 102687.
846 50. Yang, J., et al., *Overexpression of S100A4 protects retinal ganglion cells against*
847 *retinal ischemia-reperfusion injury in mice.* Exp Eye Res, 2020. **201**: p. 108281.
848 51. Lam, T., et al., *Reversal of intramyocellular lipid accumulation by lipophagy and a*
849 *p62-mediated pathway.* Cell Death Discov, 2016. **2**: p. 16061.
850 52. He, S., et al., *Review: Epigenetic mechanisms in ocular disease.* Mol Vis, 2013. **19**: p.
851 665-74.
852 53. Wang, J., Y. Li, and S. Zhang, *N(6)-methyladenosine modification: A vital role of*
853 *programmed cell death in myocardial ischemia/reperfusion injury.* Int J Cardiol, 2022.
854 **367**: p. 11-19.

855 54. Lee, D., et al., *Retinal Degeneration in a Murine Model of Retinal Ischemia by*
856 *Unilateral Common Carotid Artery Occlusion.* Biomed Res Int, 2021. **2021**: p.
857 7727648.

858

859

860 Figures and Tables

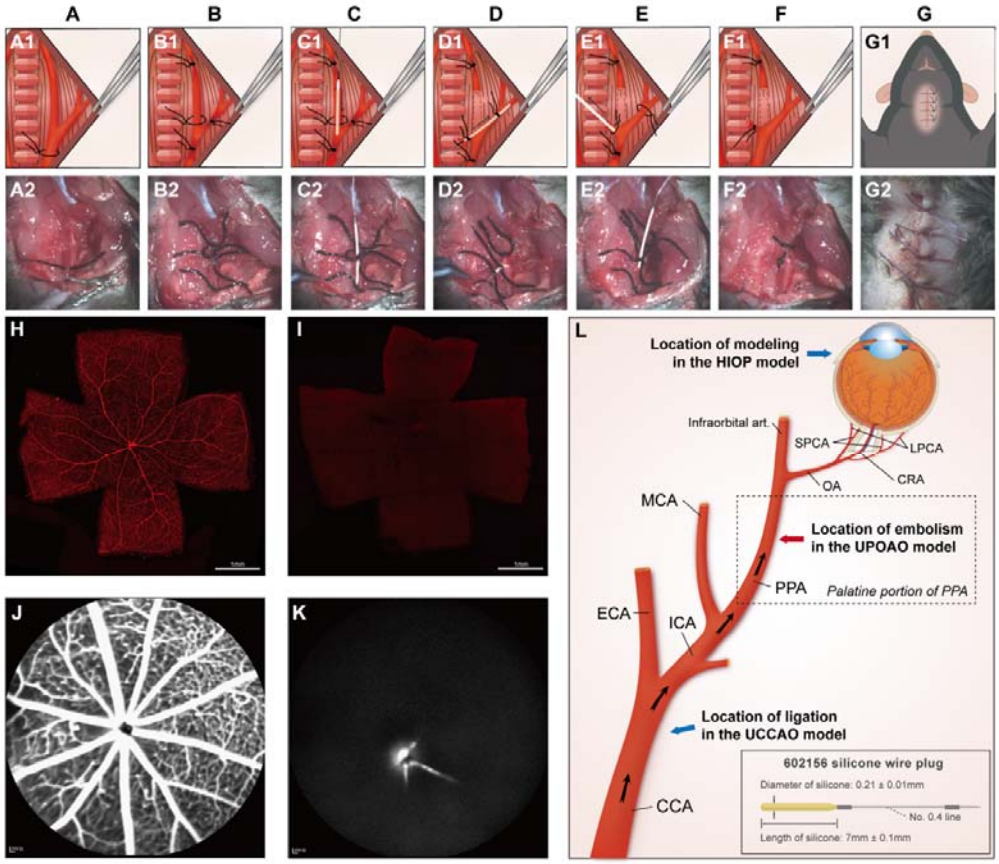

861

862 **Fig. 1 Modeling Procedure, Validation, and Cervical Artery Anatomy**

863 (A1-G1) Schematic illustration of unilateral pterygopalatine ophthalmic artery occlusion
864 (UPOAO). (A2-G2) Practical operation of UPOAO. (A1, A2) Blunt separation and
865 exposure of the left cervical arteries. (B1, B2) Arterial suture ligation. (C1, C2) Insertion of

866 the silicone wire embolus. The artery was incised to create a hole, and the silicone wire
867 embolus was inserted. (D1, D2) Artery disconnection and movement of the silicone wire
868 embolus. The artery was cut along the incision, and the silicone wire embolus was
869 retracted and reinserted. (E1, E2) Removal of the silicone wire embolus and reperfusion.
870 (F1, F2) Suture removal. The sutures at both ends of the disconnected vessel were
871 knotted, and the other two sutures were removed. (G1, G2) Anatomic reduction and
872 suturing of the skin. (H, I) Canavalin A label vasculature of the UPOAO mouse retina.
873 The silicone wire embolus was inserted into artery before perfusing rhodamine-labeled
874 canavalin A into the heart of UPOAO mouse. The sham eye served as an unpracticed
875 control eye, while the UPOAO lateral eye represented the experimental eye. Retinal
876 vessels in the sham eye (H) exhibited fluorescence filling, while retinal vessels in the
877 UPOAO lateral eye (I) remained unfilled. Scale bar = 1 mm. (J and K) Fluorescein
878 Fundus Angiography (FFA) performed before removing the silicone wire embolus from
879 the UPOAO mouse. The vessels in the sham lateral retina (J) were perfused, while the
880 lateral retinal perfusion in UPOAO (K) was delayed. (L) Schematic illustration of cervical
881 artery anatomy and ocular blood supply. Embolization of the PPA resulted in ocular
882 ischemia. The red arrow indicates the site of the silicone wire embolus occlusion. The
883 silicone wire embolus used a type 602156 wire, extended to 7mm with a diameter of
884 0.21mm. The blue arrows indicate the modelling locations of the HIOP model and the
885 UCCAO model, respectively. CCA: common carotid artery; ICA: internal carotid artery;
886 ECA: external carotid artery; PPA: pterygopalatine artery; MCA: middle cerebral artery;
887 Infraorbital art.: infraorbital artery; OA: ophthalmic artery; SPCA: short posterior ciliary

888 artery; LPCA: long posterior ciliary artery; CRA: central retinal artery.

889

890 **Table 1** Antibodies Used in Staining of Flat-Mounted Retina and Sections

Antibodies	Species	Dilution	Company
PKCα	rabbit	1:1000	Sigma
Recoverin	rabbit	1:1000	Millipore
Calbindin	rabbit	1:5000	SWANT
ChAT	goat	1:200	Millipore
Iba1	rabbit	1:500	Wako
CD45	rabbit	1:100	CST
Rhodamine-labeled canavalin A	/	1:125	MKBio
Goat anti-mouse IgG Alexa Fluor 488	goat	1:500	Jackson
Donkey anti-rabbit IgG Alexa Fluor 594	donkey	1:500	Jackson
Donkey anti-goat IgG Alexa Fluor 488	donkey	1:500	Jackson

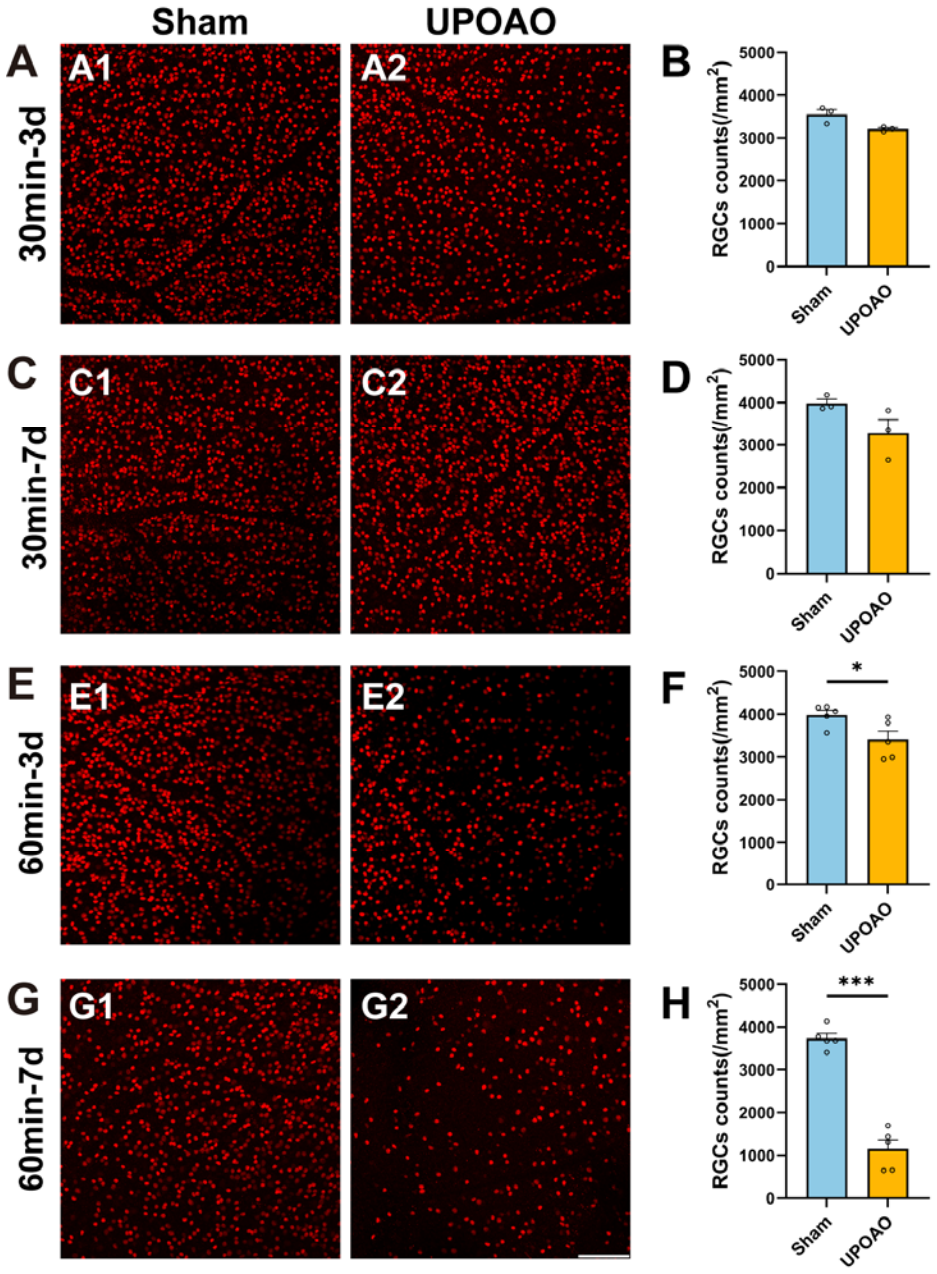

Fig. 1 Staining and Quantification of Retinal Ganglion Cells (RGCs) at Different Ischemia and Reperfusion Times.

Flat-mounted retina RGCs were labeled with Brn3a staining. (A, B) Representative pictures of the peripheral field (A), and quantification of surviving RGCs in all fields (B) in the 30-minute ischemia and 3-days reperfusion group. n = 3. (C, D) Representative pictures of the peripheral field (C), and quantification of surviving RGCs in all fields (D) in

898 the 30-minute ischemia and 7-days reperfusion group. n = 3. (E, F) Representative

899 pictures of the peripheral field (E), and quantification of surviving RGCs in all fields (F) in

900 the 60-minute ischemia and 3-days reperfusion group. n = 5. (G, H) Representative

901 pictures of the peripheral field (G), and quantification of surviving RGCs in all fields (H) in

902 the 60-minute ischemia and 7-days reperfusion group. n = 5. The results showed a

903 significant loss of RGCs after 60 minutes of ischemia. Data were presented as means ±

904 s.e.m, *: p<0.05, **: p<0.01, ***: p<0.001, ****: p<0.0001, t-test. Scale bar = 100 μm.

905

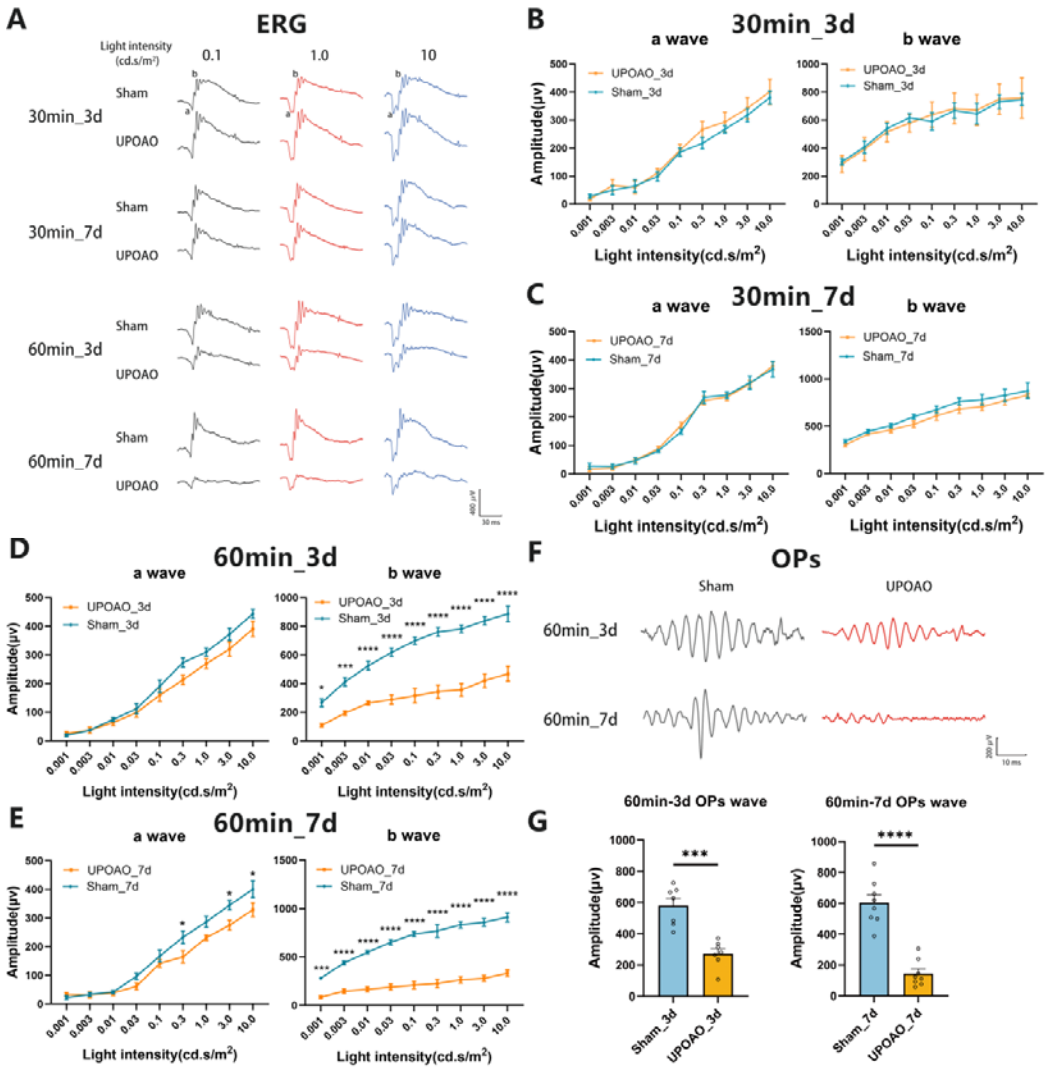

906

907 **Fig. 2 Comparison of Electroretinographic (ERG) Dark-Adapted Responses at Different**

908 **Ischemia and Reperfusion Times.**

909 Following the evaluation of surviving RGCs, visual function in sham and UPOAO

910 experimental eyes at various ischemia and reperfusion times was assessed using ERG.

911 (A) Representative waveforms in the four groups at the stimulus light intensities of 0.1,

912 1.0, and 10.0 cd.s/m2, respectively. (B) Quantification of a-wave and b-wave amplitudes

913 in the 30-minute ischemia and 3-days reperfusion group. n = 5. (C) Quantification of a-

914 wave and b-wave amplitudes in the 30-minute ischemia and 7-days reperfusion group. n

915 = 5. (D) Quantification of a-wave and b-wave amplitudes in the 60-minute ischemia and

916 3-days reperfusion group. n = 7. (E) Quantification of a-wave and b-wave amplitudes in

917 the 60-minute ischemia and 7-days reperfusion group. n = 8. Dark-adapted responses

918 showed almost similar a-wave amplitudes but significantly decreased b-wave amplitudes

919 in the 60-minute ischemia groups. The amplitudes of b-waves declined at 3-days and

920 even more prominently at 7-days. (F, G) Representative OPs and quantification of

921 amplitudes in the 60-minute ischemic groups. n = 7 in the 3-days reperfusion group; n = 8

922 in the 7-days reperfusion group. The amplitudes of OPs decreased significantly at 7-days

923 reperfusion. The decline in b-waves and OPs along with the loss of RGCs, supports the

924 selection of a 60-minute ischemic duration as an appropriate choice. Data were

925 presented as means ± s.e.m, *: $p<0.05$, **: $p<0.01$, ***: $p<0.001$, ****: $p<0.0001$, two-way

926 ANOVA test for a-waves and b-waves; paired t-test for OPs.

927

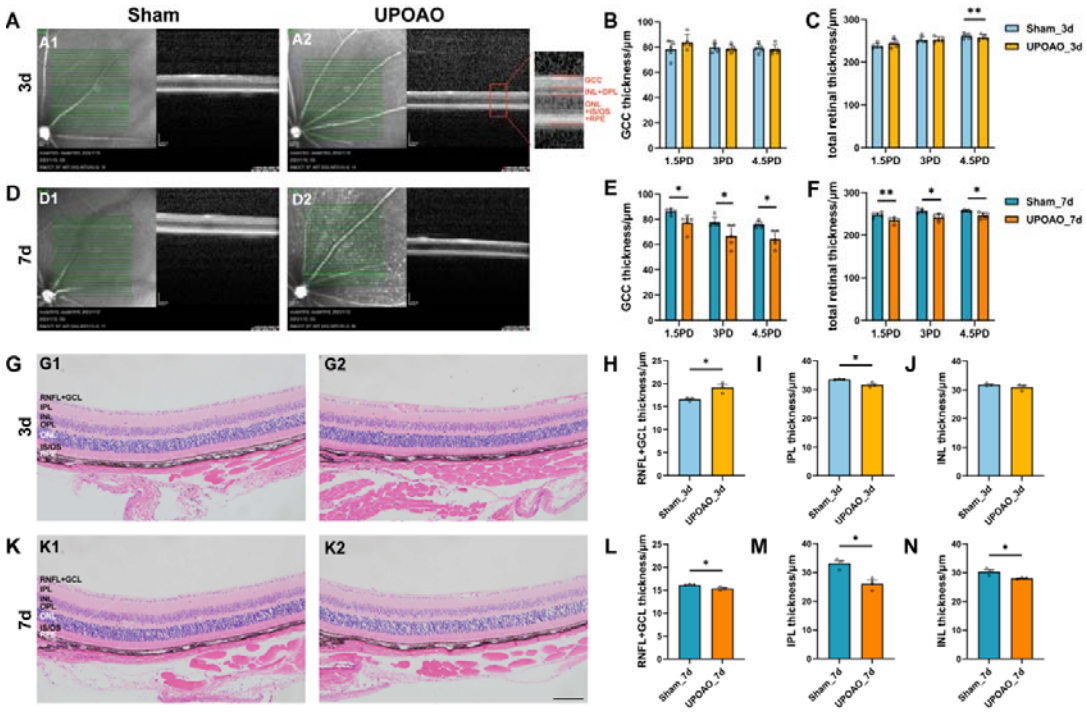

928

929 **Fig. 3 Changes in Retina Morphology in the UPOAO Model.**

930 (A) Representative OCT images of the mouse retina at 3-days. The Green lines indicate

931 the OCT scan area starting from the optic disc. Local magnification and layering are

932 annotated. GCC: ganglion cell complex, including RNFL, GCL and IPL layers. (B and C)

933 Quantification of GCC and total retinal thickness at 3-days. The thickness of the GCC

934 and the entire retina in OCT was measured and compared at distances of 1.5 PD, 3.0 PD

935 and 4.5 PD from the optic disc, respectively. n = 5. (D) Representative OCT images of

936 the mouse retina at 7-days. (E and F) Quantification of GCC and total retinal thickness at

937 7-days. n = 5. (G) Representative HE images of the mouse retina at 3-days. (H, I and J)

938 Quantification of NFL + GCL, IPL, and INL thickness at 3-days. Retinal thickness in HE

939 was measured near the optic nerve head and compared. n = 3. (K) Representative HE

940 images of the mouse retina at 7-days. (L, M and N) Quantification of NFL + GCL, IPL,

941 and INL thickness at 7-days. n = 3. Data were presented as means ± s.e.m, *: $p<0.05$, **:

942 p<0.01, ***: p<0.001, ****: p<0.0001, two-way ANOVA test in OCT and paired t-test in HE.

943 PD: papillary diameters; RNFL: retinal nerve fiber layer; GCL: ganglion cell layer; IPL:

944 inner plexiform layer; INL: inner nuclear layer; OPL: outer plexiform layer; ONL: outer

945 nuclear layer; IS: inner segment; OS outer segment; RPE: retinal pigment epithelium.

946 Scale bar = 100 μm.

947

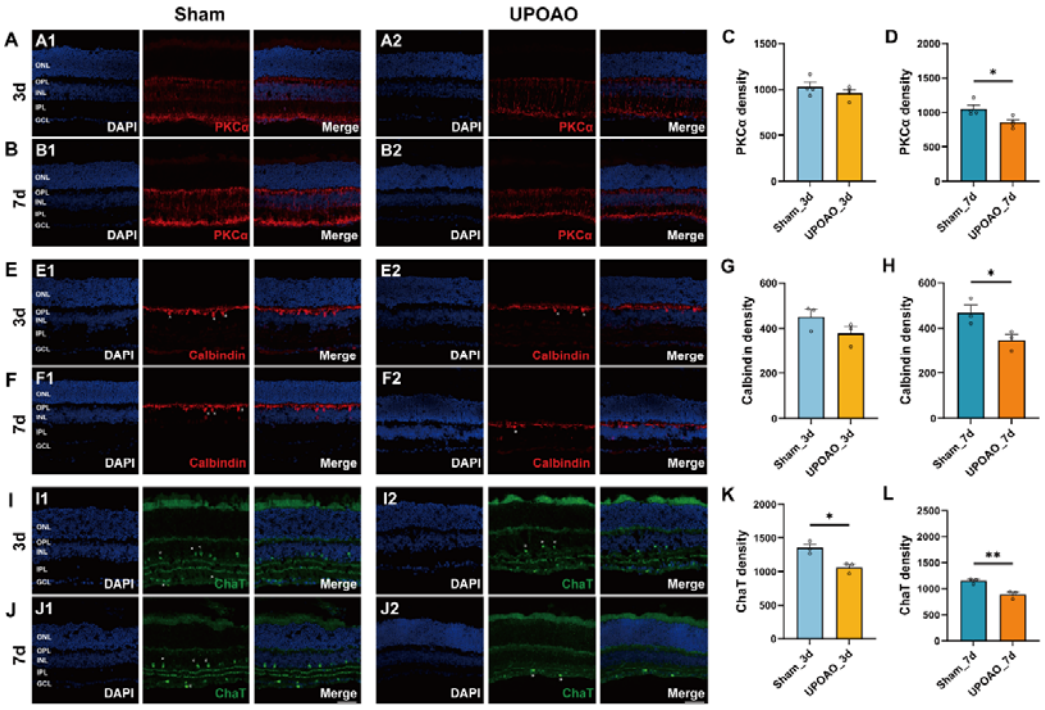

948

949 **Fig. 5 Changes in Bipolar Cells, Horizontal Cells, and Cholinergic Amacrine Cells in**

950 **UPOAO Mice.**

951 (A) Representative images of mouse retina co-stained with DAPI and PKCα at 3-days (B)

952 Representative images of mouse retina co-stained with DAPI and PKCα at 7-days. (C)

953 Quantification of PKCα fluorescence density at 3-days. (D) Quantification of PKCα

954 fluorescence density at 7-days. n = 4. (E) Representative images of mouse retina co-

955 stained with DAPI and Calbindin at 3-days. (F) Representative images of mouse retina

956 co-stained with DAPI and Calbindin at 7-days. Horizontal cell somata are indicated by
957 white asterisks. (G) Quantification of Calbindin fluorescence density at 3-days. (H)
958 Quantification of Calbindin fluorescence density at 7-days. n = 3. (I) Representative
959 images of mouse retina co-stained with DAPI and ChAT at 3-days. (J) Representative
960 images of mouse retina co-stained with DAPI and ChAT at 7-days. Cholinergic amacrine
961 cell somata are indicated by white asterisks. (K) Quantification of ChAT fluorescence
962 density at 3-days. (L) Quantification of ChAT fluorescence density at 7-days. n = 3. Data
963 were presented as means ± s.e.m, *: $p<0.05$, **: $p<0.01$, ***: $p<0.001$, t- test. Scale bar =
964 50 μm.

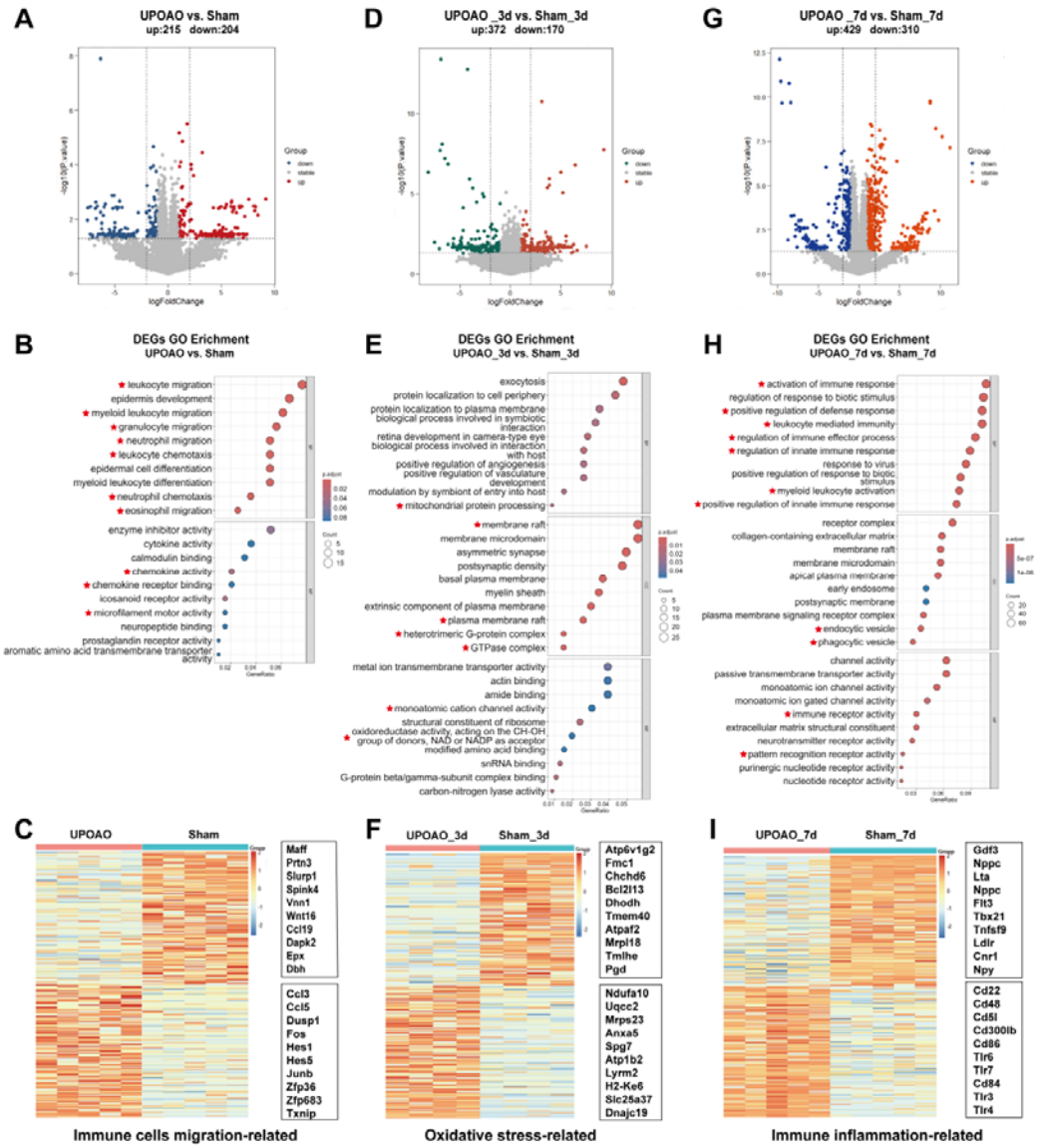

Fig. 6 Transcriptomic Features at Different Times of Reperfusion.

RNA-seq evaluation was performed at 0-day, 3-days, and 7-days reperfusion periods in UPOAO revealing enrichment in pathways related to immune cells migration, oxidative stress, and immune inflammation. (A, D, G) Volcano plots display differential expression genes (DEGs) between UPOAO and sham eyes in the no-perfusion group (A), 3-days perfusion group (D), and 7-days perfusion group (G), respectively. Red dots: significant upregulated genes, green and blue dots: significant downregulated genes, grey dots:

973 stable expressed genes, adjusted $P < 0.05$. log2FC = 1. (B, E, H) Gene ontology (GO)
974 analysis of differential genes in the non-perfusion group (B), 3-days group (E), and 7-
975 days group (H). The DEGs between UPOAO and sham eyes were enriched in pathways
976 associated with immune cells migration (0d), oxidative stress (3d), and immune
977 inflammation (7d), respectively. (C, F, I) Heatmap displaying the top 100 downregulated
978 and top 100 upregulated DEGs between UPOAO and sham at non-perfusion, 3-days,
979 and 7-days reperfusion, respectively. The box represents the genes related to immune
980 cells migration (C), oxidative stress (F), and immune inflammation (I). The ranking was
981 determined by the magnitude of fold change. In each heatmap, the upper box represents
982 the top 10 downregulated genes, while the lower box represents the top 10 upregulated
983 genes.
984

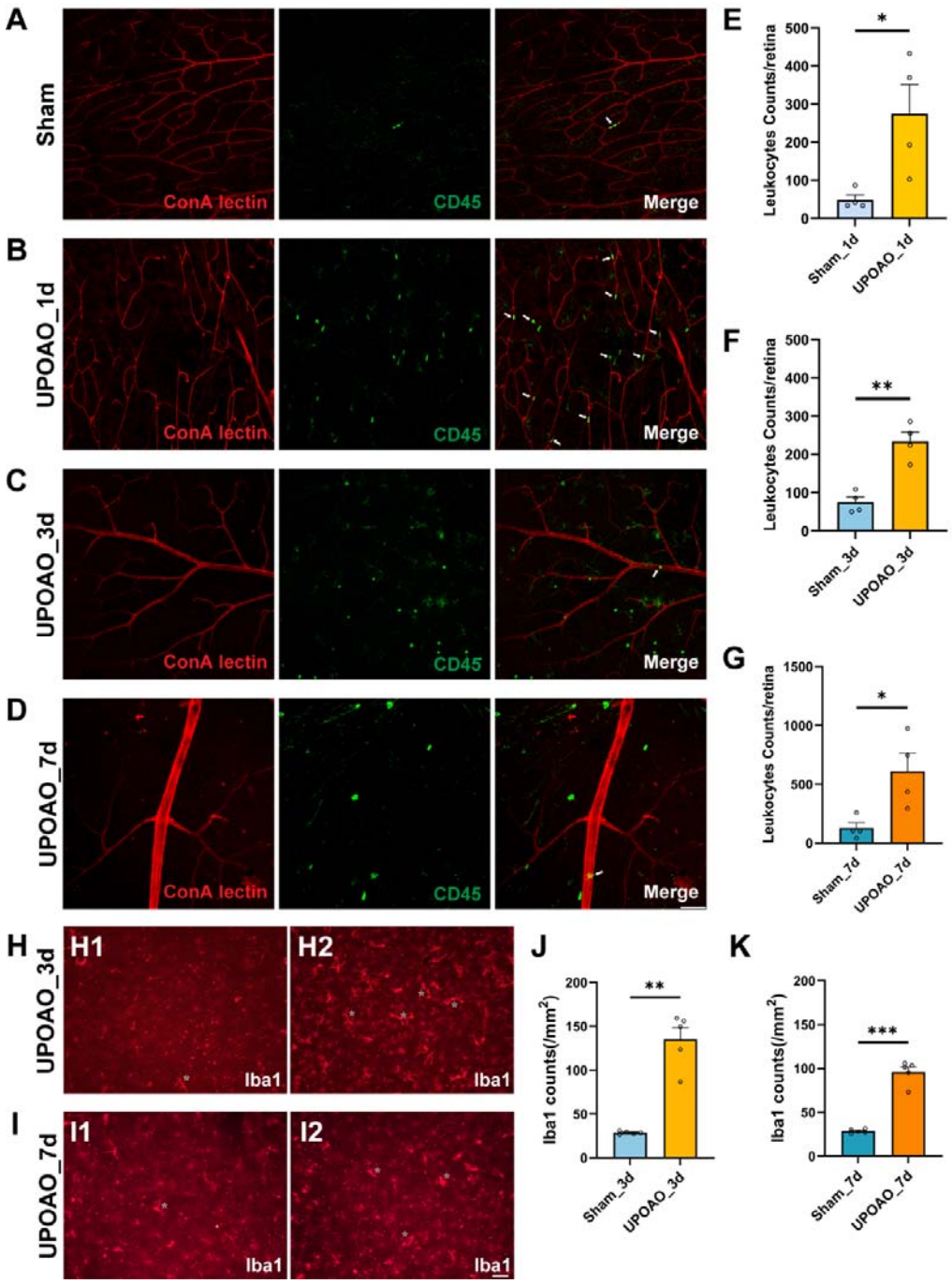

985

986 **Fig. 7 Peripheral Leukocyte Infiltration and Retinal Resident Microglial Activation.**

987 Rhodamine-labeled canavalin A was used for immediate cardiac perfusion to visualize

988 blood vessels, followed by CD45 immunofluorescent staining to observe the relationship

989 between blood vessels and $CD45^+$ cells in sham (A), 1-day perfusion group (B), 3-days

990 perfusion group (C), and 7-days perfusion group (D). The presence of $CD45^+$ cells within
991 blood vessels is indicated by white arrows. Scale bar = 50 μm. $CD45^+$ cell counts were
992 performed in whole retinas of 1-day (E), 3-days (F), 7-days (G). The cellular morphology
993 and distribution of microglial cells in the superficial retina were assessed in 3-days (H)
994 and 7-days (I). Activated microglial cells are indicated by white asterisks. Microglial cell
995 counting was conducted in the superficial retina of 3-days (J) and 7-days (K). Data points
996 for $CD45^+$ cells were derived from four flat-mounted retinas, and data points for microglial
997 cells were from five flat-mounted retinas. Data were presented as means ± s.e.m, *:
998 $p<0.05$, **: $p<0.01$, ***: $p<0.001$, ****: $p<0.0001$, t- test. Scale bar = 50 μm.
999

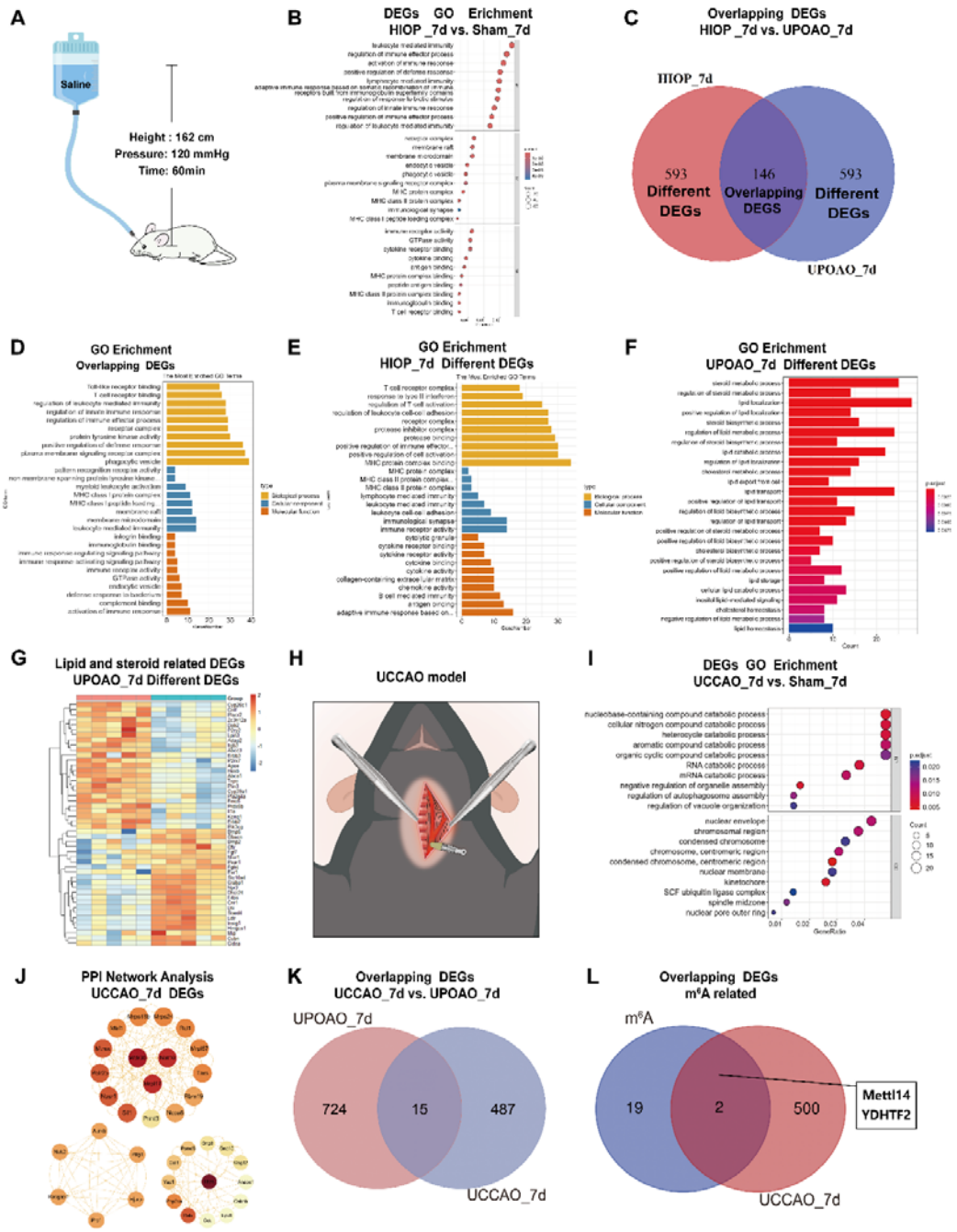

Fig. 8 Transcriptomic Results Comparison between UPOAO, HIOP, and UCCAO Models. RNA-seq comparison between UPOAO and extravascular occlusion models: HIOP and UCCAO. (A) Schematic illustration of the HIOP model. (B) GO analysis of differential expression genes (DEGs) in the HIOP model at 7-days perfusion. (C) Venn diagram indicating the overlapping DEGs (146 genes) between HIOP and UPOAO models, as

1006 well as the remaining DEGs specific to each group (593 genes in each group). (D) GO
1007 analysis of the overlapping DEGs between HIOP and UPOAO models. (E) GO analysis
1008 of the remaining DEGs in the HIOP model at 7-days perfusion, excluding the overlapping
1009 DEGs. (F) GO analysis of the remaining DEGs, excluding the overlapping DEGs. (G)
1010 Heatmap showing the inter-sample distribution of lipid and steroid-related DEGs from the
1011 analysis of the remaining DEGs in the UPOAO model. (H) Schematic illustration of the
1012 UCCAO model. (I) GO analysis of DEGs in the UCCAO model. (J) Hub genes identified
1013 through protein-protein interaction (PPI) network analysis of the DEGs in the UCCAO
1014 model. (K) Venn diagram indicating the overlapping DEGs between UCCAO and UPOAO
1015 models (15 genes). (L) Venn diagram indicating the presence of two overlapping DEGs
1016 between UCCAO DEGs and m6A-related genes.
1017

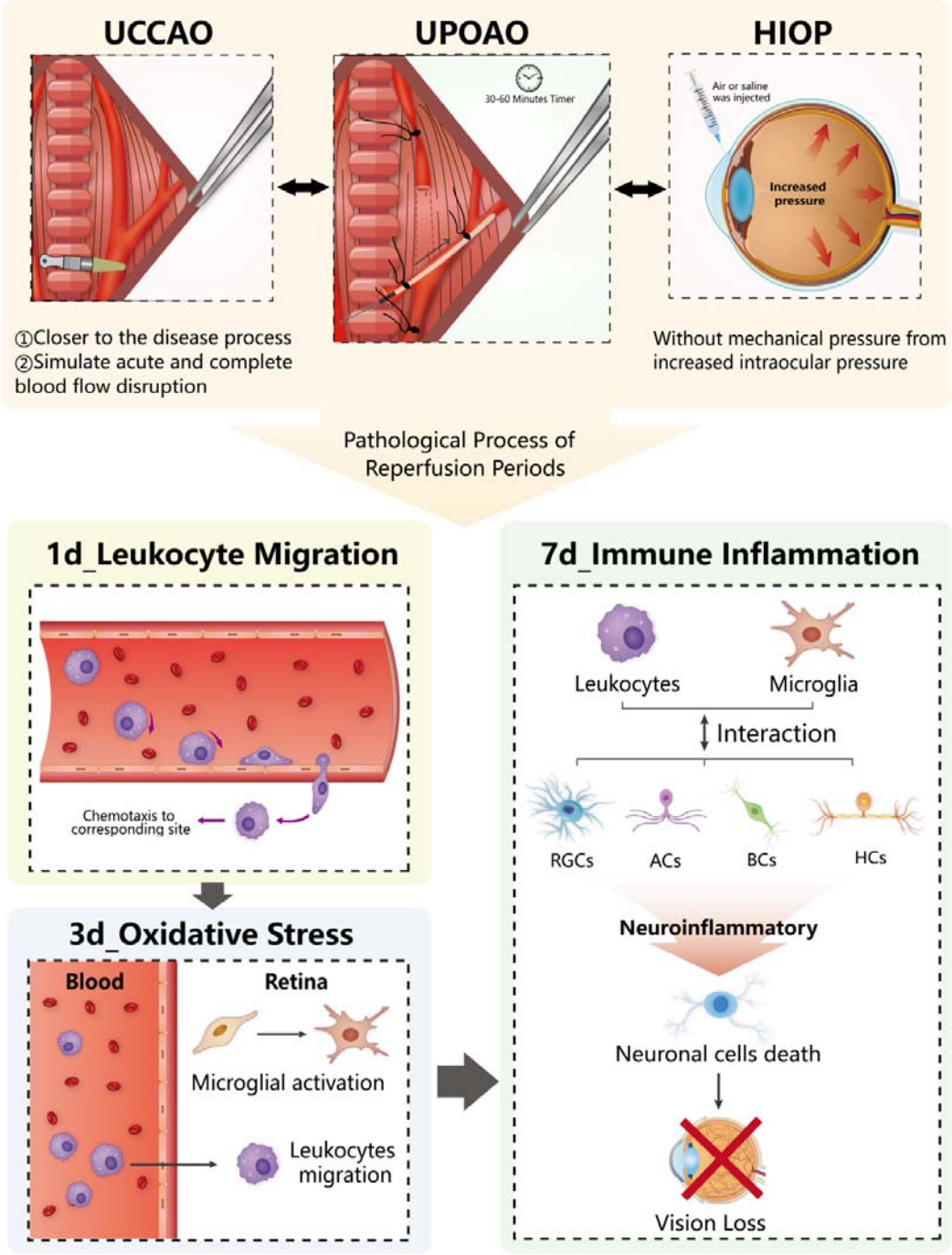

Fig. 9 The Characteristic Features of UPOAO Model during Ischemia-Reperfusion Periods.

1023

1024

1025

1026

1027 **Supplementary data**

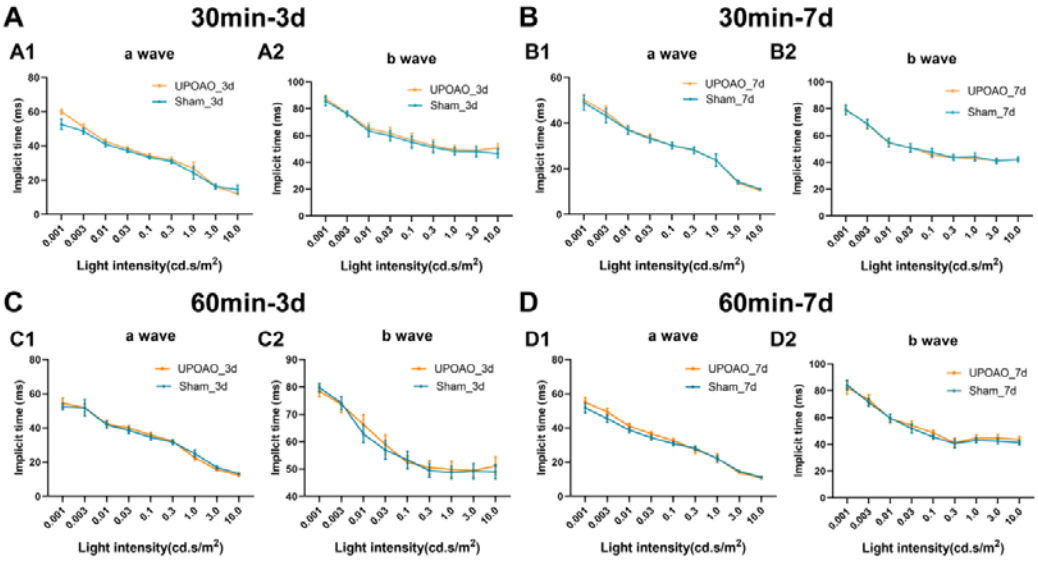

1028

1029 **Fig.S1 Response Times of a-Waves and b-Waves in ERG at Different Light Intensities.**

1030 (A, B) Response times of a-waves and b-waves were measured under different light

1031 intensities at 3-days and 7-days post-UPOAO in the 30-minutes ischemia group. n = 5. (C, D)

1032 Response times of a-waves and b-waves were measured under different light intensities at 3-

1033 days and 7-days post-UPOAO in the 60-minute ischemia group. n = 7 at 3-days; n = 8 at 7-

1034 days. Data were presented as means ± s.e.m, *: $p<0.05$, **: $p<0.01$, ***: $p<0.001$, ****:

1035 $p<0.0001$, two-way ANOVA test.

1036

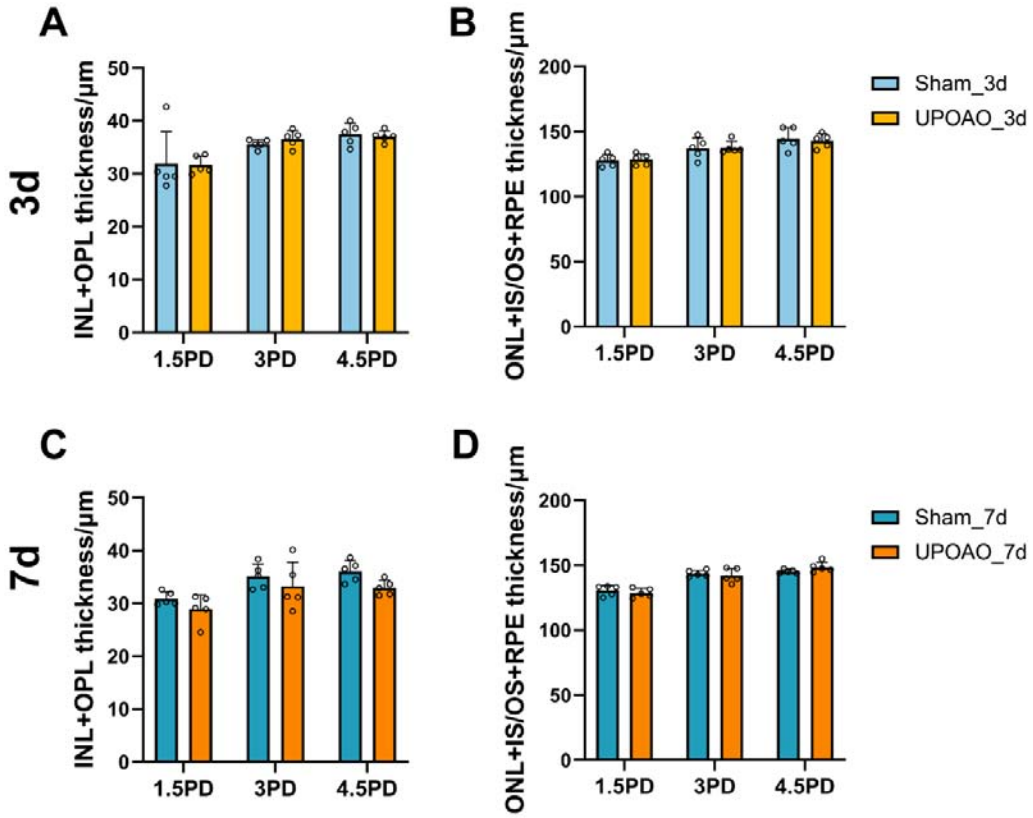

1037

1038 **Fig.S2 Quantification of INL+OPL Thickness and ONL+IS/OS+RPE Thickness in OCT during**

1039 **3-days and 7-days Reperfusion of UPOAO Animals.**

1040 The INL+OPL thickness and the ONL+IS/OS+RPE thickness were measured and compared

1041 at distances of 1.5 PD, 3.0 PD and 4.5 PD from the optic disc using OCT. (A and B)

1042 Quantification of INL+OPL layer thickness (A) and ONL+IS/OS+RPE layer thickness (B) at 3-

1043 days. n = 5. No significant differences were observed. (C and D) Quantification of INL+OPL

1044 layer thickness (C) and ONL+IS/OS+RPE layer thickness (D) at 7-days. n = 5. No significant

1045 differences were observed. Data were presented as means ± s.e.m, *: $p<0.05$, **: $p<0.01$, ***:

1046 $p<0.001$, ****: $p<0.0001$, two-way ANOVA test.

1047

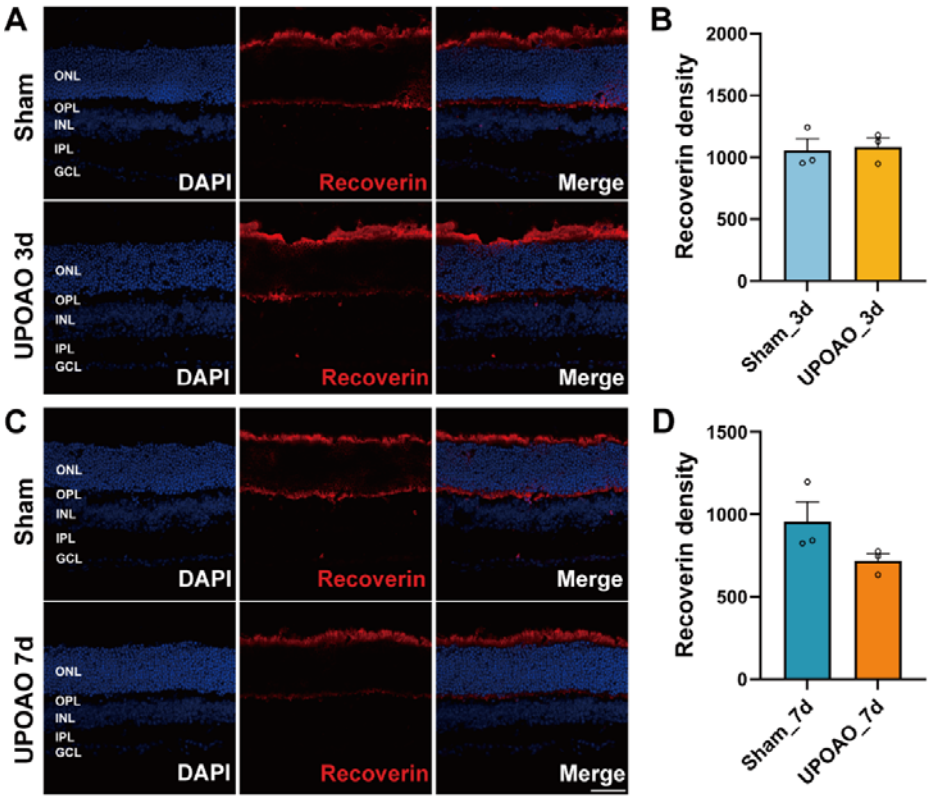

Fig.S3 Changes in Photoreceptor Cells in UPOAO.

(A) Representative images of mouse retina co-stained with DAPI and Recoverin at 3-days. (B) Representative images of mouse retina co-stained with DAPI and Recoverin at 7-days. n = 3. Data were presented as means ± s.e.m, *: $p<0.05$, **: $p<0.01$, ***: $p<0.001$, ****: $p<0.0001$, t-test. Scale bar = 50 μm.

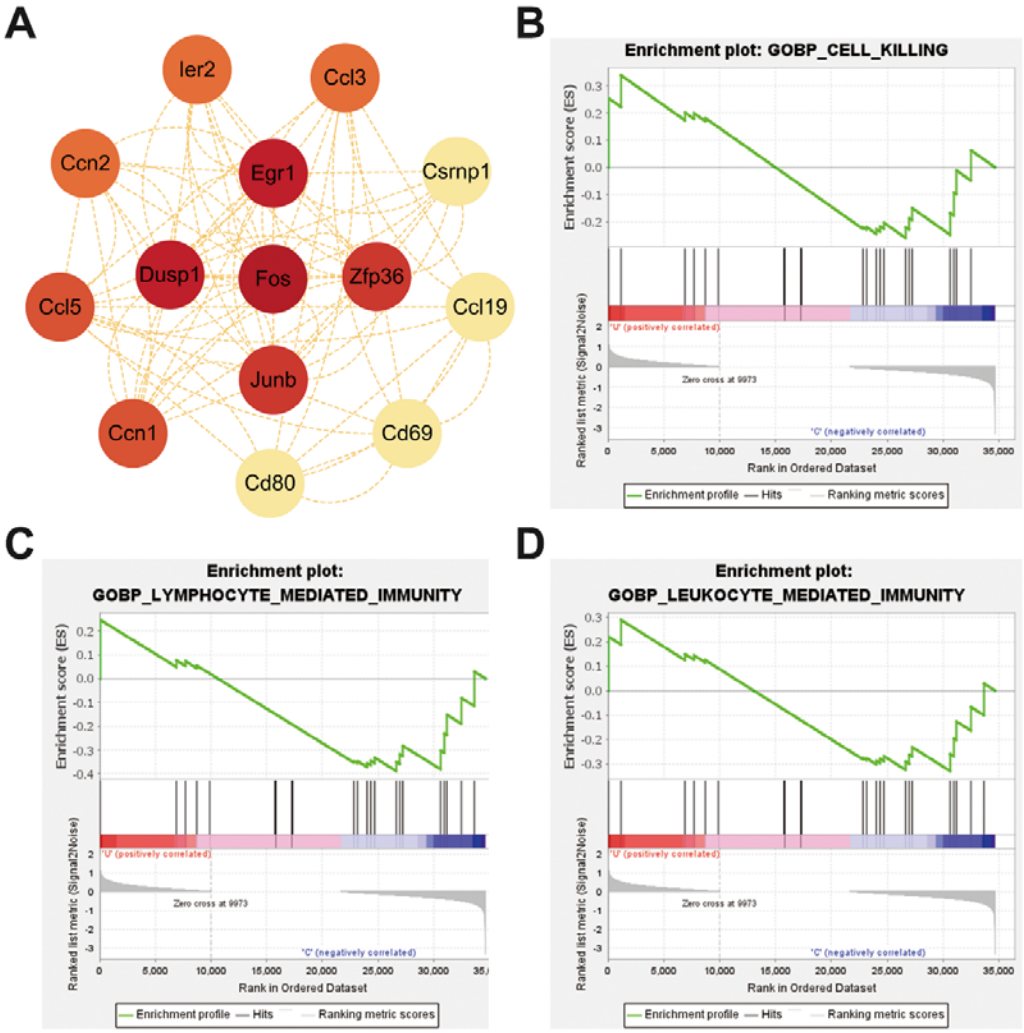

Fig.S4 Hub Genes in PPI Analysis and Gene Set Enrichment Analysis (GSEA) during the Non-Reperfusion Stage in UPOAO.

(A) Hub genes identified through PPI analysis of DEGs in the non-reperfusion group. (B-D) GSEA analysis of the pathway of the cell killing (B), lymphocyte mediated-immunity (C), and leukocyte mediated-immunity (D) in the non-reperfusion group.

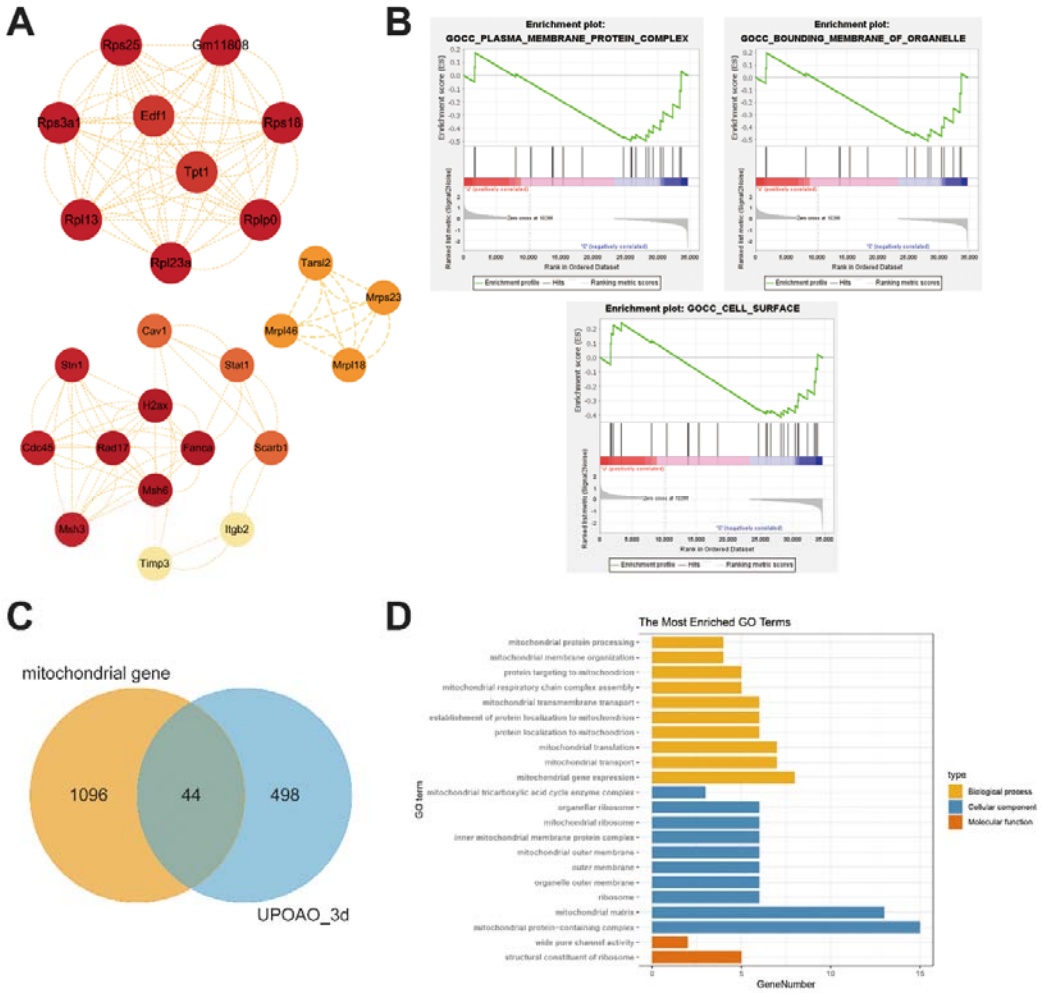

Fig.S5 Hub Genes, GSEA Analysis at 3-days Reperfusion in UPOAO, and Relation with Mitochondrial Genes.

(A) Hub genes identified through PPI analysis of DEGs in the 3-days reperfusion group. (B) GSEA analysis of the pathways related to plasma membrane protein complex (top left), bounding membrane of organelle (top right), and cell surface (bottom). (C) Venn diagram showing the overlapping genes between mitochondrial genes and DEGs at 3-days reperfusion (44 genes). (D) GO analysis of the 44 overlapping DEGs.

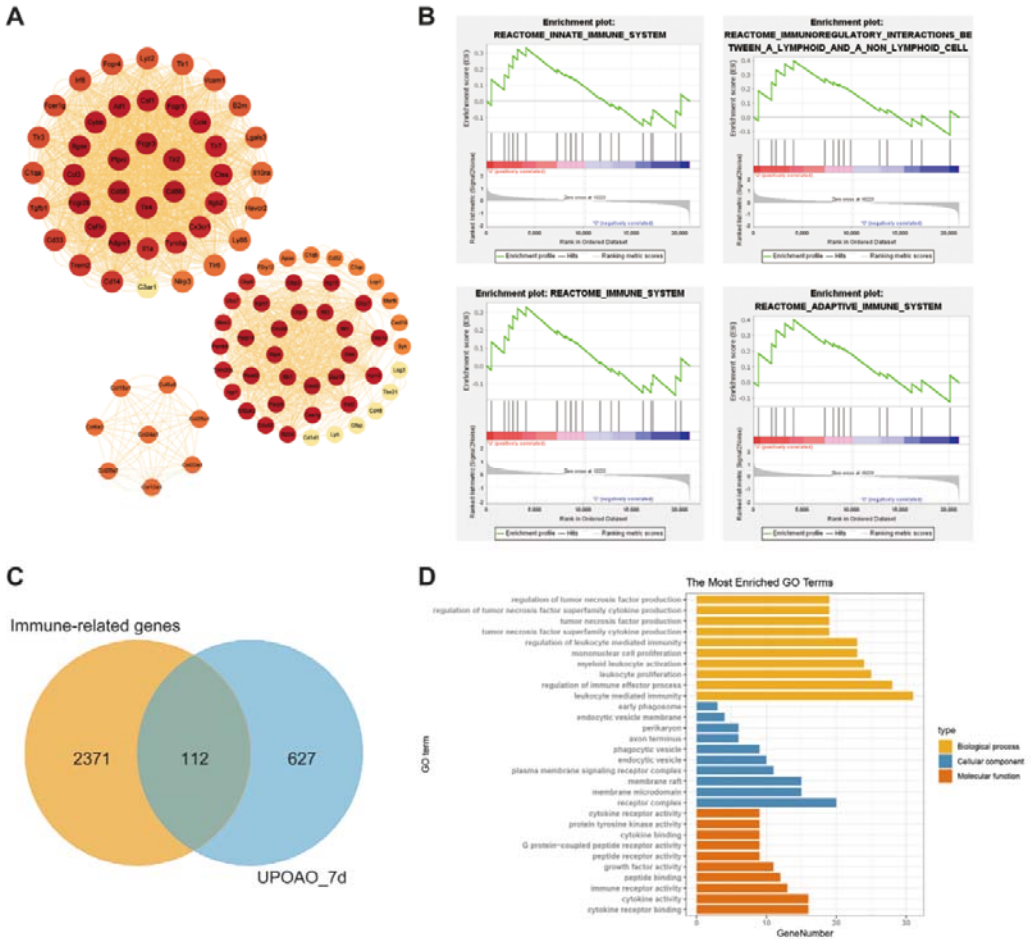

Fig.S6 Hub Genes, GSEA Analysis at 7-days Reperfusion in UPOAO, and Relation with Immune Genes.

(A) Hub genes identified through PPI analysis of DEGs in the 7-days reperfusion group. (B) GSEA analysis of the pathways related to the reactome innate immune system (top left), reactome immunoregulatory interactions between a lymphoid and a non-lymphoid cell (top right), reactome immune system (bottom left), and reactome adaptive immune system (bottom right). (C) Venn diagram showing the overlapping genes between immune genes and DEGs at 7-days reperfusion (112 genes). (D) GO analysis of the 112 overlapping DEGs.

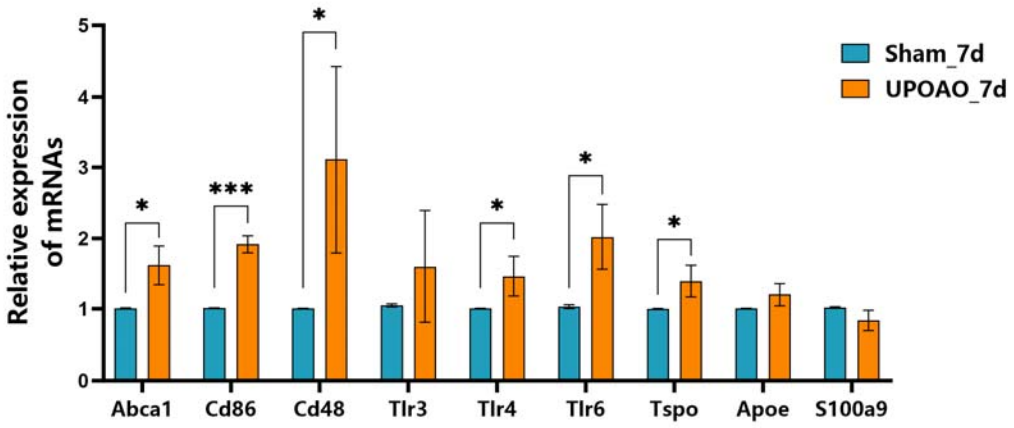

1080

1081 **Fig.S7 Upregulation of Immune Inflammation-Related Gene Expression in the 7-days**

1082 **Reperfusion Group.**

1083 The genes Abca1, Cd86, Cd48, Tlr4, Tlr6, and Tspo were significantly upregulated in the

1084 7-days reperfusion group, while other immune-inflammatory and chemotaxis-related

1085 genes showed no significant differences. The data points were from the retina of four

1086 animals. Data were presented as means ± s.e.m, *: p<0.05, **: p<0.01, ***: p<0.001, ****:

1087 p<0.0001, Paired t-test.

1088

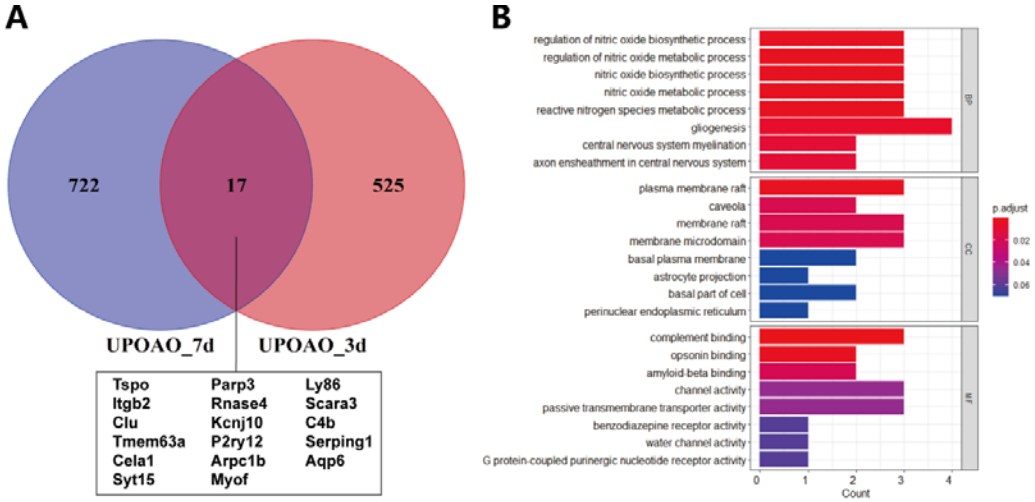

1089

1090 **Fig.S8 Co-Expressed Genes during 3-days and 7-days Reperfusion.**

1091 (A) Venn diagram showing the overlap of DEGs between the 3-days and 7-days

1092 reperfusion groups, along with a list of the 17 overlapping DEGs. (B) GO analysis of the

1093 17 overlapping DEGs.

1094

1095

1096

1097

1098

1099

1100 **Table. S1 Primers Used in This Study.**

Gene Name		Sequence (5'->3')
Tlr3	Forward primer	CGATTCCCGACCAGCACTCT
	Reverse primer	CACATTTCCTTTCAGCCTGTGAT
Tlr4	Forward primer	TCCCTGCATAGAGGTAGTTCC
	Reverse primer	TCAAGGGGTTGAAGCTCAGA
Cd48	Forward primer	GGAACTGGATTTCAAGGTCATTCA
	Reverse primer	ATGGTCCAAGTGGGTCCTTAT
Ldlr	Forward primer	CCAATCGACTCACGGGTTCA
	Reverse primer	ACAGTGTCGACTTCTCTAGGC
Cd86	Forward primer	ATGGACCCCAGATGCACCA
	Reverse primer	TGTGCCCAAATAGTGCTCGT
Tspo	Forward primer	ACTGTATTCAGCCATGGGGTATG
	Reverse primer	CCAAGGGAACCATAGCGTCC
Abca1	Forward primer	GCAAGGCCGCACCATTATTT
	Reverse primer	TCTGAGAAACACTGTCCTCCTTTT
Apoe	Forward primer	CGGGTGCTCTGTTTTGGAGA
	Reverse primer	GGCTAGGCATCCTGTCAGC

S100a9	Forward primer	TGGCAACCTTTATGAAGAAAGAGA
	Reverse primer	GTGGGTTGTTCTCATGCAGC
β-actin	Forward primer	CACTGTCGAGTCGCGTCC
	Reverse primer	TCATCCATGGCGAACTGGTG

1101

1102 **Table. S2 Summary Table:** Time Course of all the Morphological, Functional, Cellular,

1103 and Transcriptome Changes in the UPOAO Model.

Changes in each group		30min-3d	30min-7d	60min-0d	60min-3d			60min-7d		
RGCs counts		-	-	/	↓			↓		
ERG	Amplitudes of a-waves	-	-	/	-			- (0.001, 0.003, 0.01, 0.03, 0.1, 1.0 cd.s/m^2) ↓ (0.3, 3.0, 10.0 cd.s/m^2)		
	Response time of a-waves	-	-		-			-		
	Amplitudes of b-waves	-	-		↓			↓		
	Response time of b-waves	-	-		-			-		
	Amplitudes of OPs-waves		/		↓			↓		
OCT					1.5 PD	3 PD	4.5 PD	1.5 PD	3 PD	4.5 PD
	GCC thickness		/		-	-	-	↓	↓	↓
	INL+OPL thickness				-	-	-	-	-	-
	ONL+IS/OS+RPE thickness				-	-	-	-	-	-
	total retinal thickness				-	-	↓	↓	↓	↓
HE	RNFL+GCL thickness		/			↑			↓	
	IPL thickness					↓			↓	
	INL thickness					-			↓	
	OPL thickness					-			-	
	ONL thickness					-			-	
	IS/OS+RPE thickness					-			-	

Changes in each group		30min-3d	30min-7d	60min-0d	60min-3d	60min-7d
Retina neural cells	Bipolar cells (PKCα)		/		-	↓
	Horizontal cells (Calbindin)				-	↓
	Cholinergic amacrine cells (ChAT)				↓	↓
	Photoreceptor cells (Recoverin)				-	-
Peripheral leukocyte infiltration (CD45)#			/		↑	↑
Microglia counts (Iba1)			/		↑	↑
RNA-seq	DEGs number		/	419 (up: 215; down: 204)	542 (up: 372; down: 170)	739 (up: 429; down: 310)
	Enrichment			Immune cells migration-related pathways	Oxidative stress-related pathways	Immune inflammation-related pathways

-: no change;

↑: increase;

↓: decrease;

/: not involved in the article;

#: supplementary content: also increase after 60min-ischemia and 1d-reperfusion;

Video 1. Blunt Dissection of Cervical Vessels. The neck was exposed, and the cervical

1111 arteries were separated using blunt dissection techniques.

1112 **Video 2. Insertion of Silicone Wire Embolus and Induction of Ischemia.** The silicone wire

1113 embolus was inserted into the PPA, initiating the ischemic condition. PPA: the

1114 pterygopalatine artery.

1115 **Video 3. Extraction of Silicone Wire Embolus and Reperfusion.** The silicone wire embolus

1116 was removed, allowing reperfusion to occur. The mouse's wound was sutured, and

1117 standard feeding procedures were followed.

1118

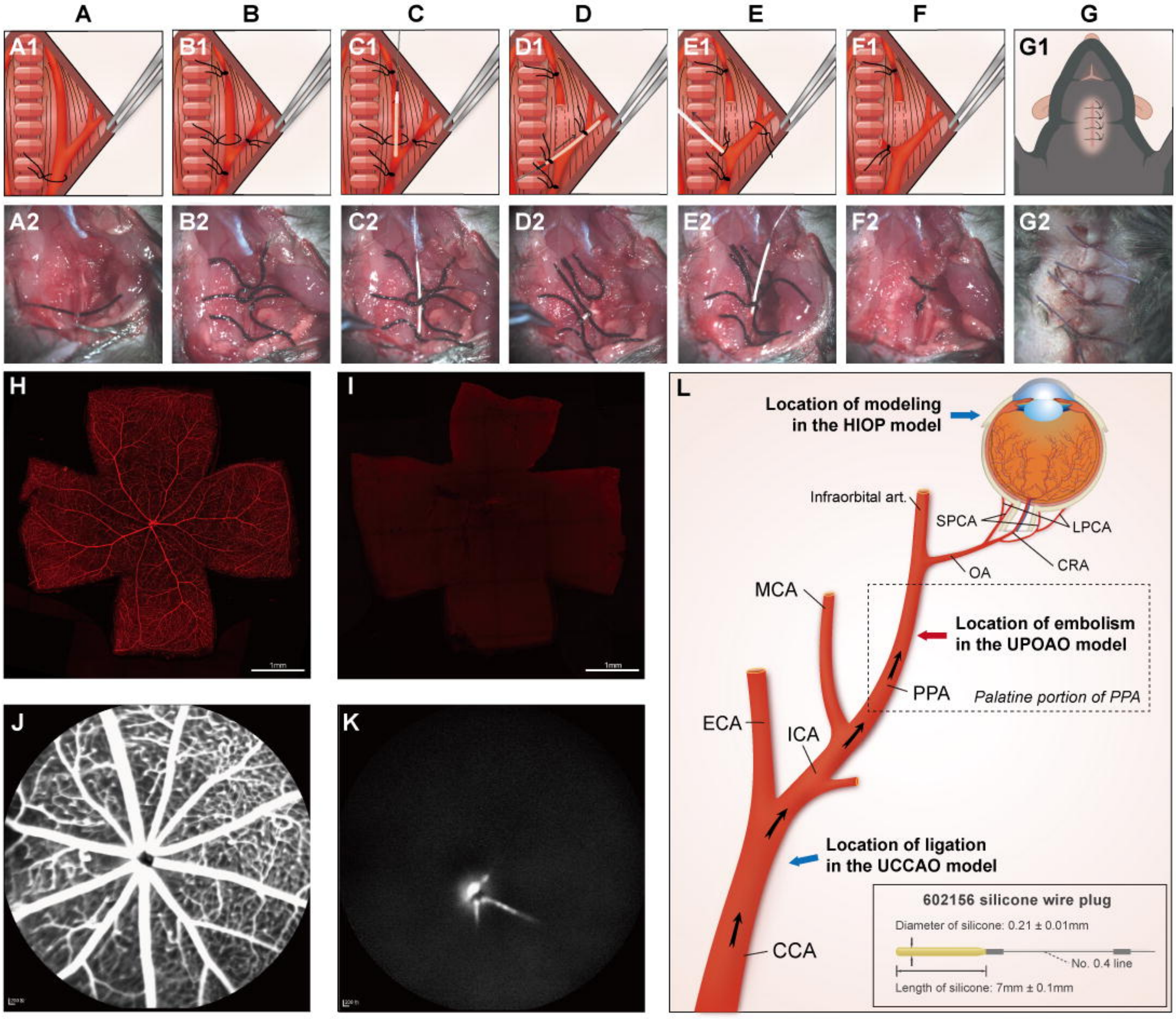
A
B
C
D
E
F
G
A1
B1
C1
D1
E1
F1
G1
A2
B2
C2
D2
E2
F2
G2
H
I
J
K
L
1mm
1mm
Location of modeling
in the HIOP model
Infraorbital art.
SPCA
LPCA
CRA
OA
MCA
Location of embolism
in the UPOAO model
PPA
Palatine portion of PPA
ECA
ICA
Location of ligation
in the UCCAO model
CCA
602156 silicone wire plug
Diameter of silicone: 0.21 ± 0.01mm
No. 0.4 line
Length of silicone: 7mm ± 0.1mm

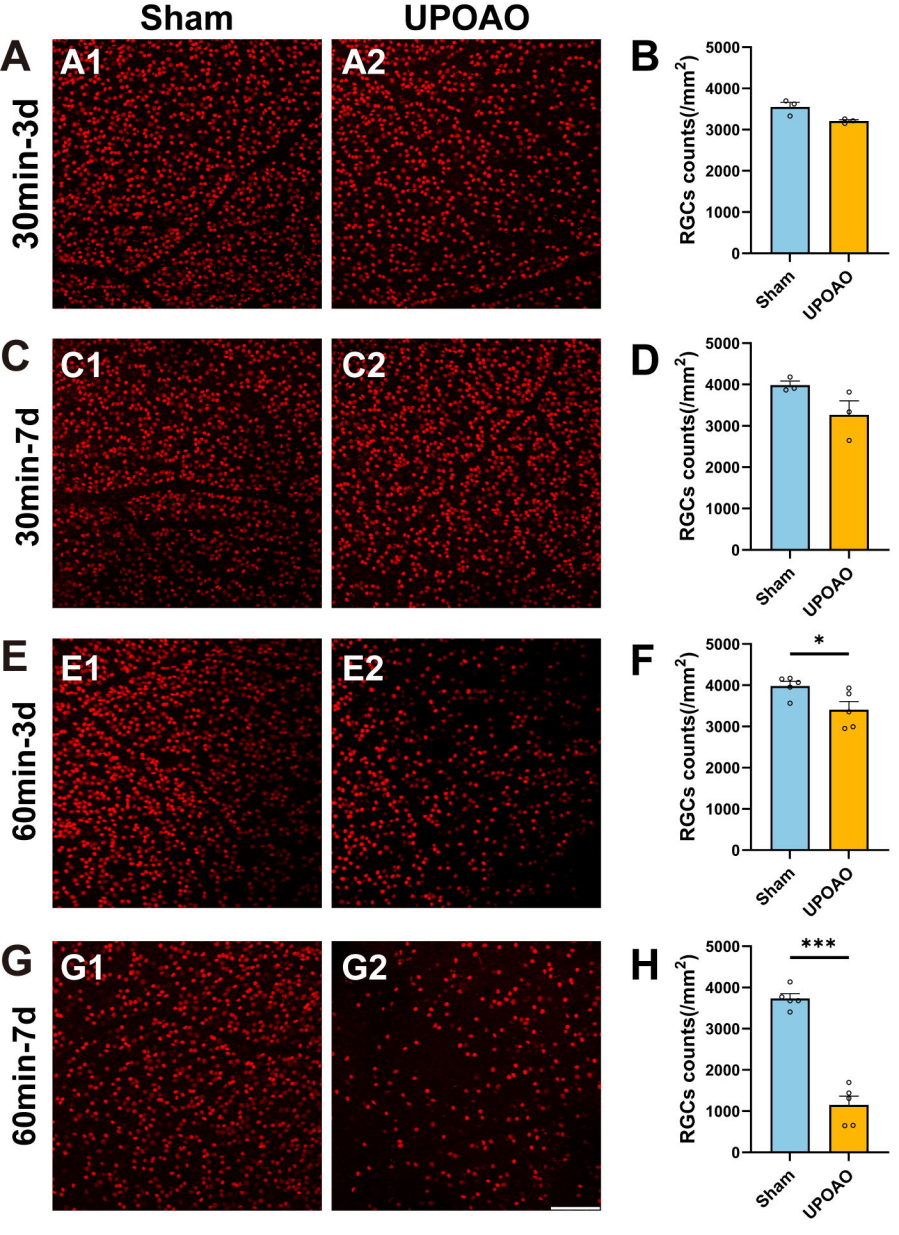
Sham
UPOAO
A
A1
A2
30min-3d
B
RGCs counts(/mm²)
5000
4000
3000
2000
1000
0
Sham
UPOAO
C
C1
C2
30min-7d
D
RGCs counts(/mm²)
5000
4000
3000
2000
1000
0
Sham
UPOAO
E
E1
E2
60min-3d
F
*
RGCs counts(/mm²)
5000
4000
3000
2000
1000
0
Sham
UPOAO
G
G1
G2
60min-7d
H
***
RGCs counts(/mm²)
5000
4000
3000
2000
1000
0
Sham
UPOAO

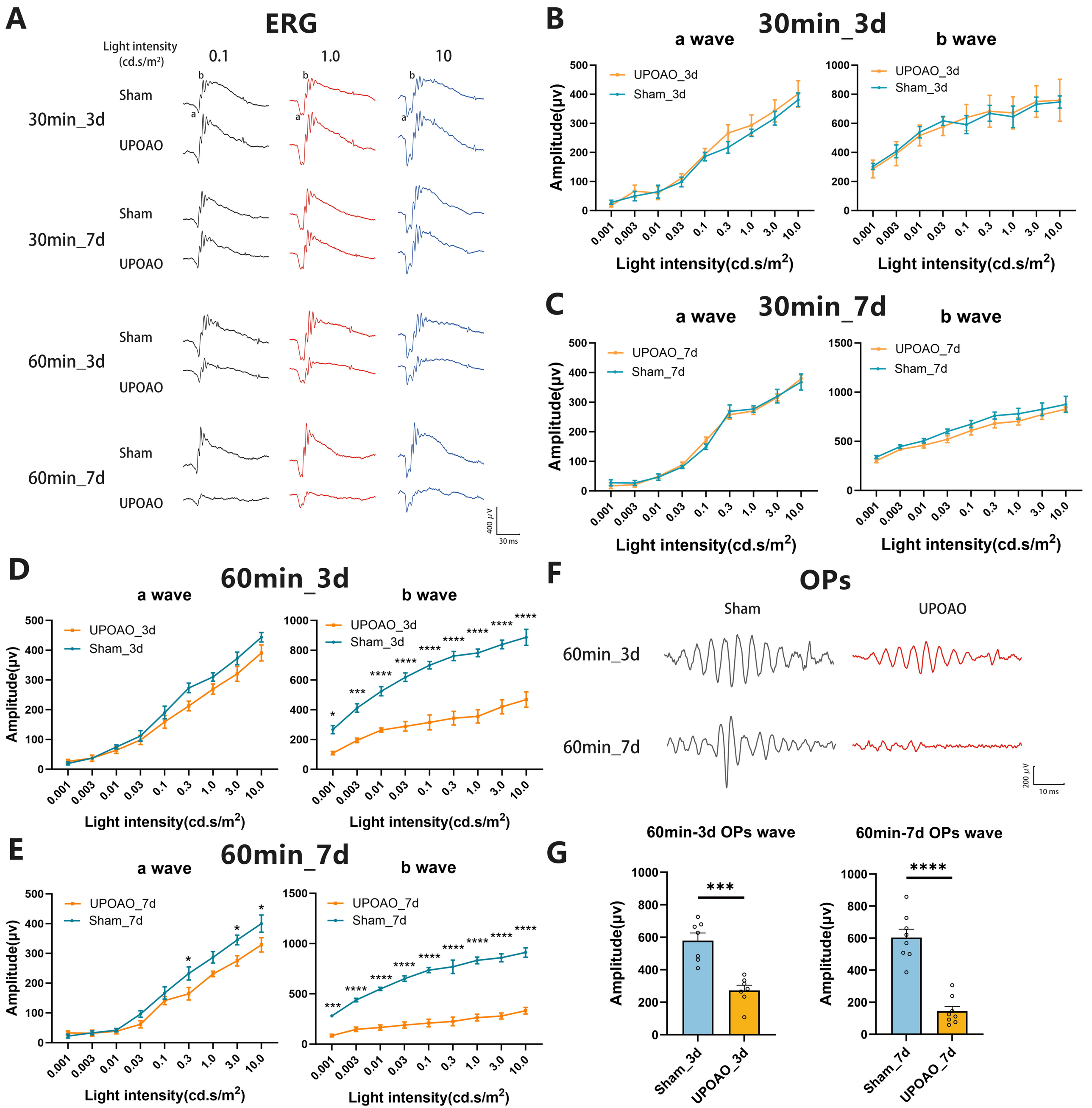
A
ERG
Light intensity (cd.s/m²)
0.1
1.0
10
30min_3d
Sham
UPOAO
30min_7d
60min_3d
60min_7d
400 μV
30 ms
B
30min_3d
a wave
b wave
UPOAO_3d
Sham_3d
Amplitude(μv)
Light intensity(cd.s/m²)
C
30min_7d
UPOAO_7d
Sham_7d
D
60min_3d
E
60min_7d
F
OPs
60min_3d
60min_7d
200 μV
10 ms
G
60min-3d OPs wave
60min-7d OPs wave
Sham_3d
UPOAO_3d
Sham_7d
UPOAO_7d

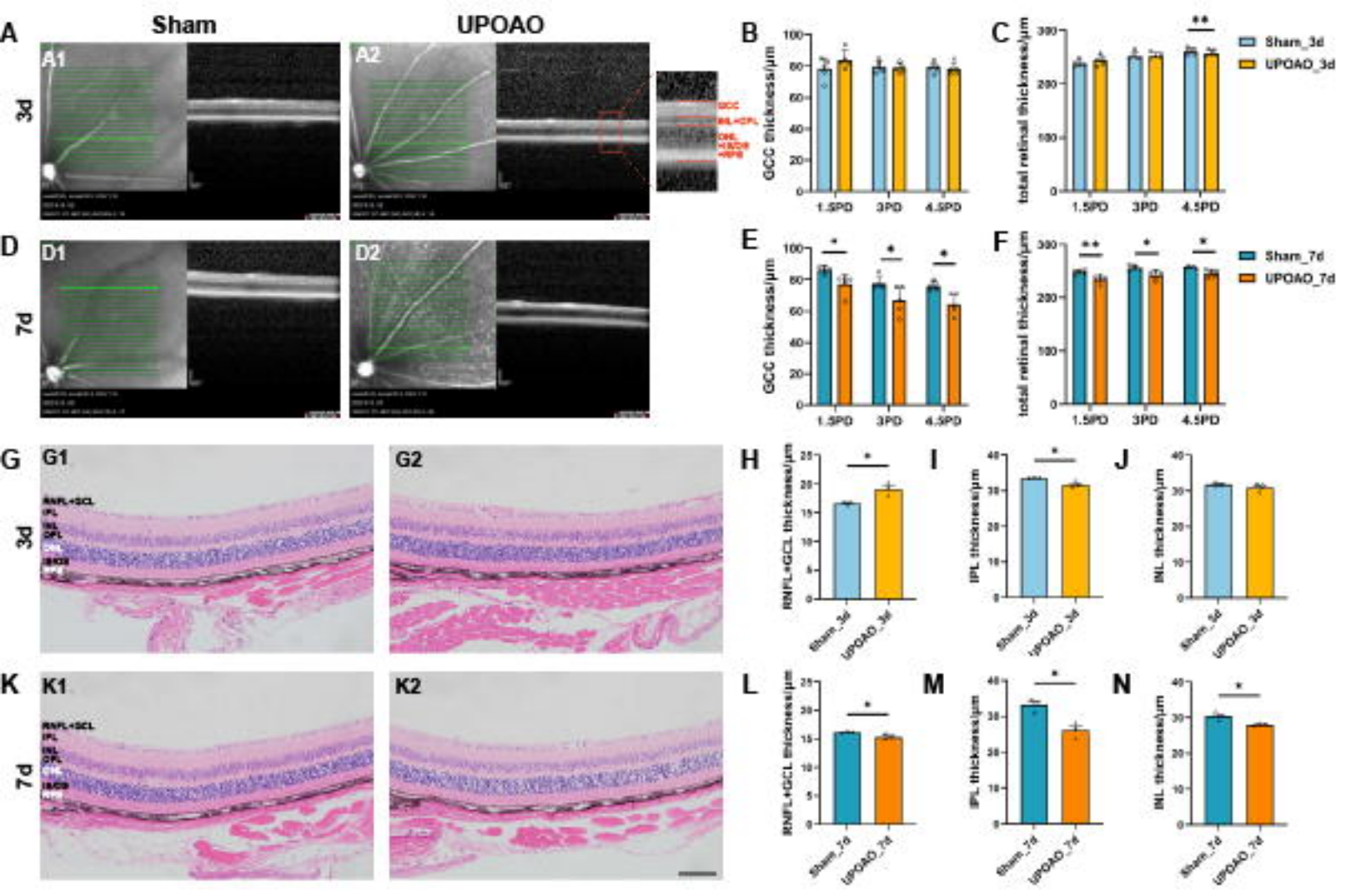

A
Sham
UPOAO
3d
A1
A2
B
GCC thickness/μm
1.5PD
3PD
4.5PD
C
total retinal thickness/μm
Sham_3d
UPOAO_3d
D
7d
D1
D2
E
F
Sham_7d
UPOAO_7d
G
G1
G2
H
RNFL+GCL thickness/μm
I
IPL thickness/μm
J
INL thickness/μm
K
K1
K2
L
M
N

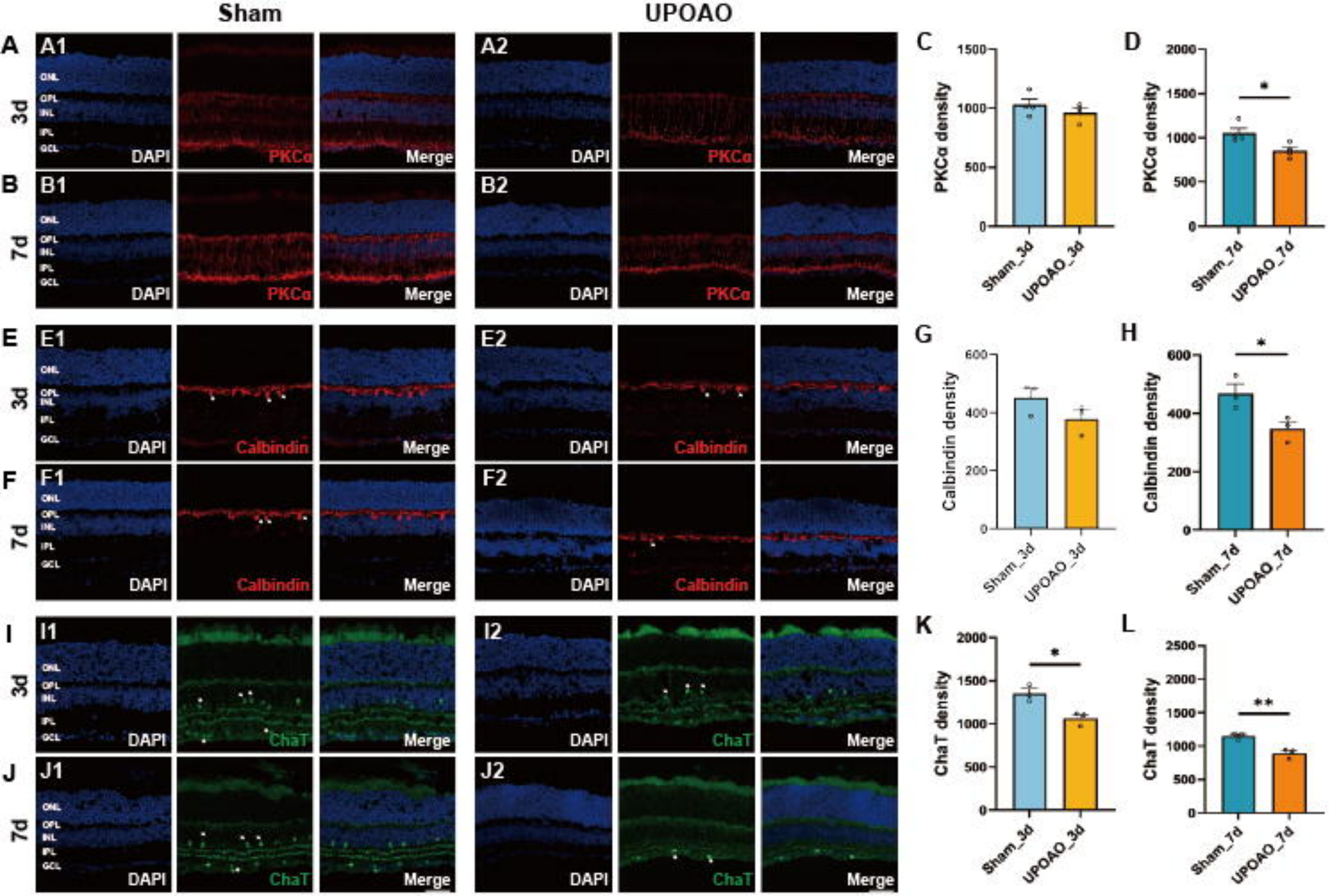
Sham
UPOAO
A
A1
A2
3d
ONL
OPL
INL
IPL
GCL
DAPI
PKCα
Merge
B
B1
B2
7d
C
PKCα density
1500
1000
500
0
Sham_3d
UPOAO_3d
D
PKCα density
2000
1500
1000
500
0
*
Sham_7d
UPOAO_7d
E
E1
E2
Calbindin
F
F1
F2
G
Calbindin density
600
400
200
0
H
Calbindin density
*
I
I1
I2
ChaT
J
J1
J2
K
ChaT density
2000
1500
1000
500
0
*
L
ChaT density
2500
2000
1500
1000
500
0
**

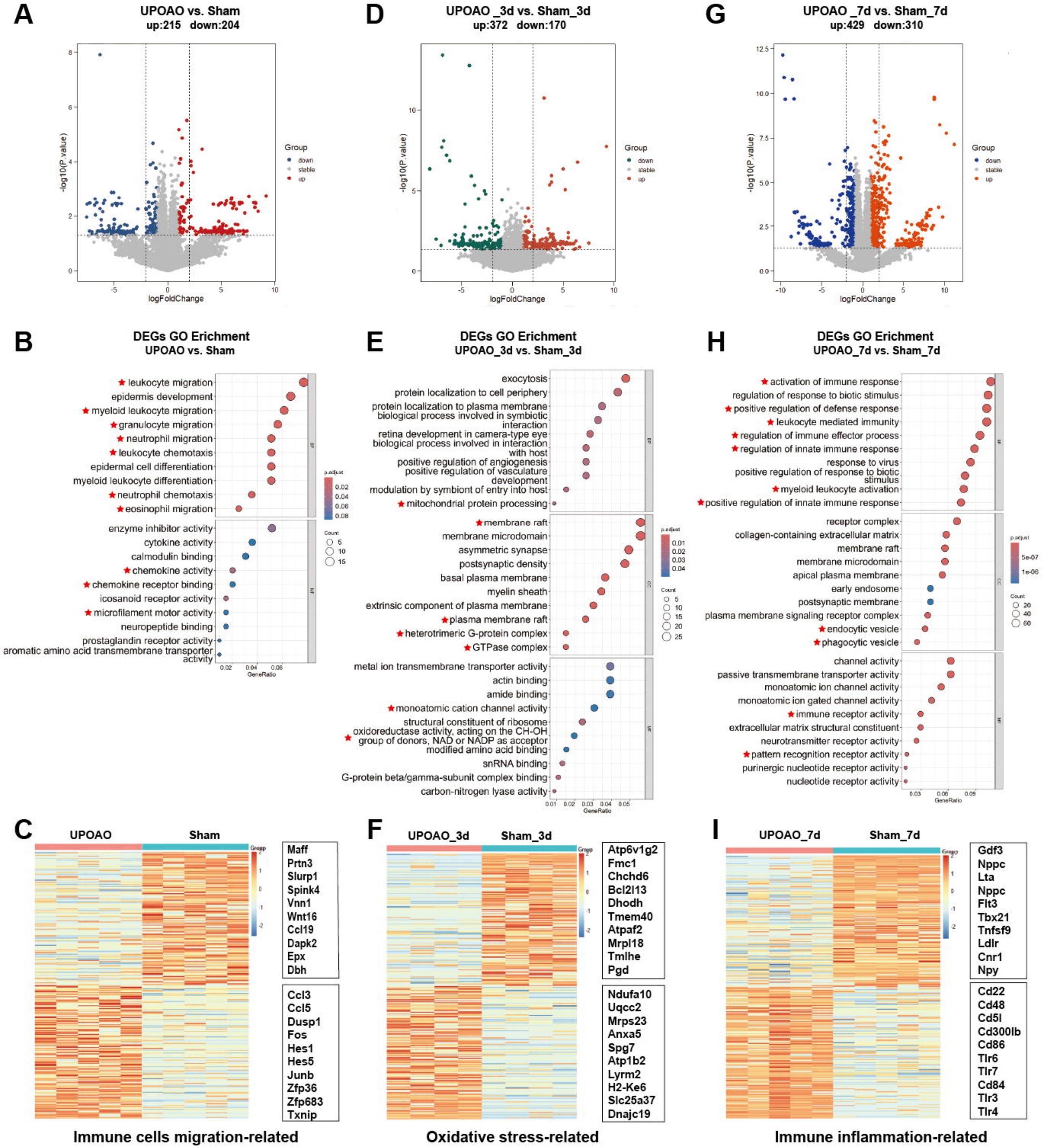
A
UPOAO vs. Sham
up:215 down:204
-log10(P.value)
logFoldChange
Group
down
stable
up
D
UPOAO _3d vs. Sham_3d
up:372 down:170
G
UPOAO _7d vs. Sham_7d
up:429 down:310
B
DEGs GO Erichment
UPOAO vs. Sham
leukocyte migration
epidermis development
myeloid leukocyte migration
granulocyte migration
neutrophil migration
leukocyte chemotaxis
epidermal cell differentiation
myeloid leukocyte differentiation
neutrophil chemotaxis
eosinophil migration
enzyme inhibitor activity
cytokine activity
calmodulin binding
chemokine activity
chemokine receptor binding
icosanoid receptor activity
microfilament motor activity
neuropeptide binding
prostaglandin receptor activity
aromatic amino acid transmembrane transporter activity
GeneRatio
p.adjust
Count
E
DEGs GO Erichment
UPOAO_3d vs. Sham_3d
exocytosis
protein localization to cell periphery
protein localization to plasma membrane
biological process involved in symbiotic interaction
retina development in camera-type eye
biological process involved in interaction with host
positive regulation of angiogenesis
positive regulation of vasculature development
modulation by symbiont of entry into host
mitochondrial protein processing
membrane raft
membrane microdomain
asymmetric synapse
postsynaptic density
basal plasma membrane
myelin sheath
extrinsic component of plasma membrane
plasma membrane raft
heterotrimeric G-protein complex
GTPase complex
metal ion transmembrane transporter activity
actin binding
amide binding
monoatomic cation channel activity
structural constituent of ribosome
oxidoreductase activity, acting on the CH-OH group of donors, NAD or NADP as acceptor
modified amino acid binding
snRNA binding
G-protein beta/gamma-subunit complex binding
carbon-nitrogen lyase activity
H
DEGs GO Erichment
UPOAO_7d vs. Sham_7d
activation of immune response
regulation of response to biotic stimulus
positive regulation of defense response
leukocyte mediated immunity
regulation of immune effector process
regulation of innate immune response
response to virus
positive regulation of response to biotic stimulus
myeloid leukocyte activation
positive regulation of innate immune response
receptor complex
collagen-containing extracellular matrix
membrane raft
membrane microdomain
apical plasma membrane
early endosome
postsynaptic membrane
plasma membrane signaling receptor complex
endocytic vesicle
phagocytic vesicle
channel activity
passive transmembrane transporter activity
monoatomic ion channel activity
monoatomic ion gated channel activity
immune receptor activity
extracellular matrix structural constituent
neurotransmitter receptor activity
pattern recognition receptor activity
purinergic nucleotide receptor activity
nucleotide receptor activity
C
UPOAO
Sham
Maff
Prtn3
Slurp1
Spink4
Vnn1
Wnt16
Ccl19
Dapk2
Epx
Dbh
Ccl3
Ccl5
Dusp1
Fos
Hes1
Hes5
Junb
Zfp36
Zfp683
Txnip
Immune cells migration-related
F
UPOAO_3d
Sham_3d
Atp6v1g2
Fmc1
Chchd6
Bcl2l13
Dhodh
Tmem40
Atpaf2
Mrpl18
Tmlhe
Pgd
Ndufa10
Uqcc2
Mrps23
Anxa5
Spg7
Atp1b2
Lyrm2
H2-Ke6
Slc25a37
Dnajc19
Oxidative stress-related
I
UPOAO_7d
Sham_7d
Gdf3
Nppc
Lta
Nppc
Flt3
Tbx21
Tnfsf9
Ldlr
Cnr1
Npy
Cd22
Cd48
Cd5l
Cd300lb
Cd86
Tlr6
Tlr7
Cd84
Tlr3
Tlr4
Immune inflammation-related

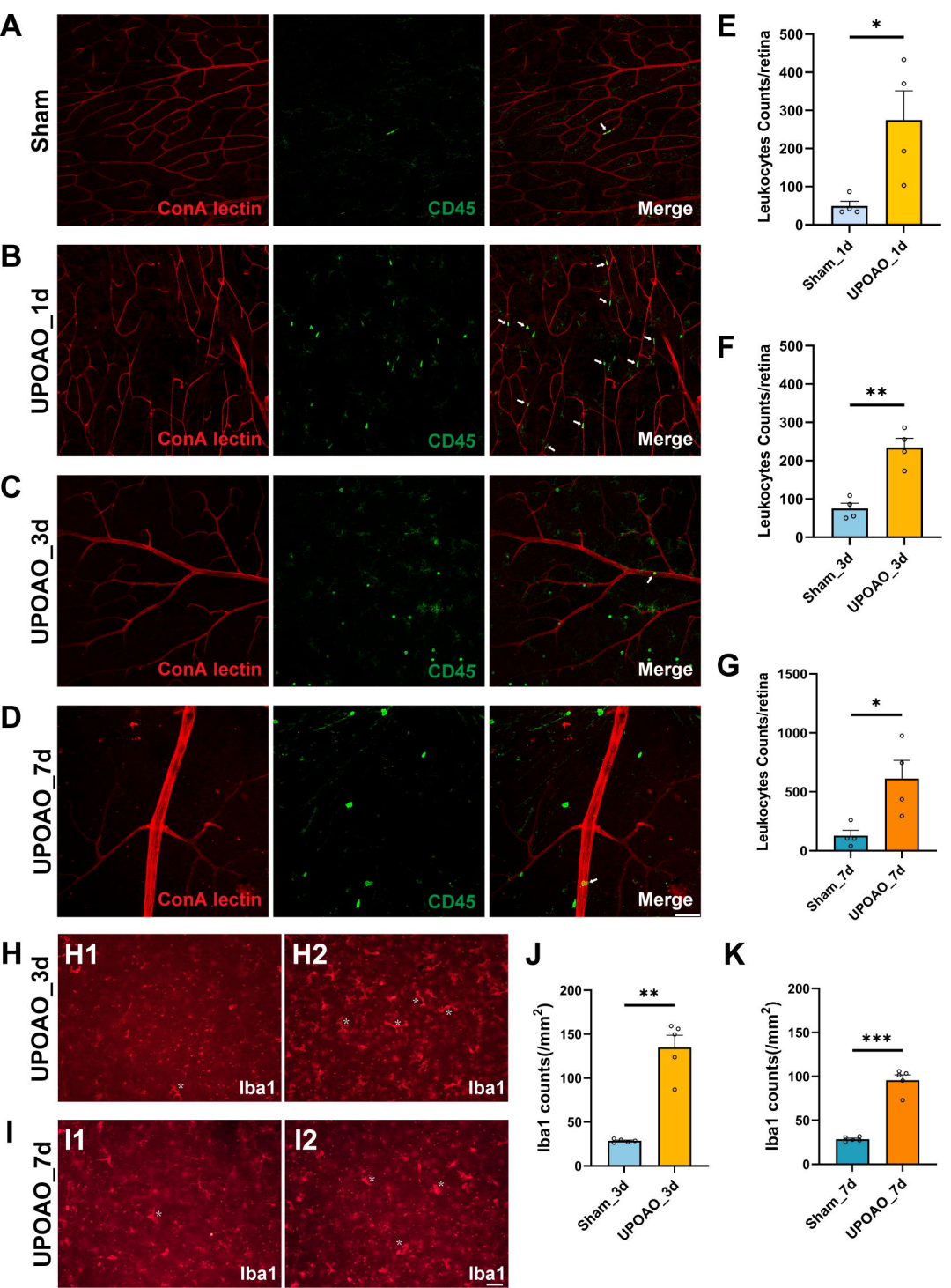
A
Sham
ConA lectin
CD45
Merge
B
UPOAO_1d
ConA lectin
CD45
Merge
C
UPOAO_3d
ConA lectin
CD45
Merge
D
UPOAO_7d
ConA lectin
CD45
Merge
E
Leukocytes Counts/retina
500
400
300
200
100
0
*
Sham_1d
UPOAO_1d
F
Leukocytes Counts/retina
500
400
300
200
100
0
**
Sham_3d
UPOAO_3d
G
Leukocytes Counts/retina
1500
1000
500
0
*
Sham_7d
UPOAO_7d
H
UPOAO_3d
H1
Iba1
H2
Iba1
I
UPOAO_7d
I1
Iba1
I2
Iba1
J
Iba1 counts(/mm2)
200
150
100
50
0
**
Sham_3d
UPOAO_3d
K
Iba1 counts(/mm2)
200
150
100
50
0
***
Sham_7d
UPOAO_7d

A

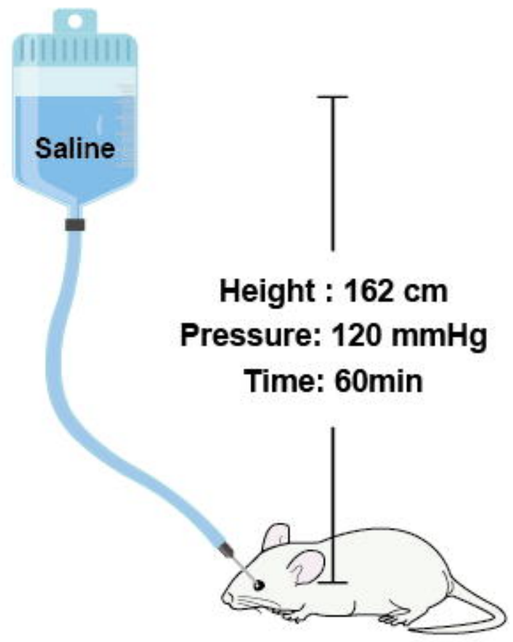

B

DEGs GO Erichment
HIOP _7d vs. Sham_7d

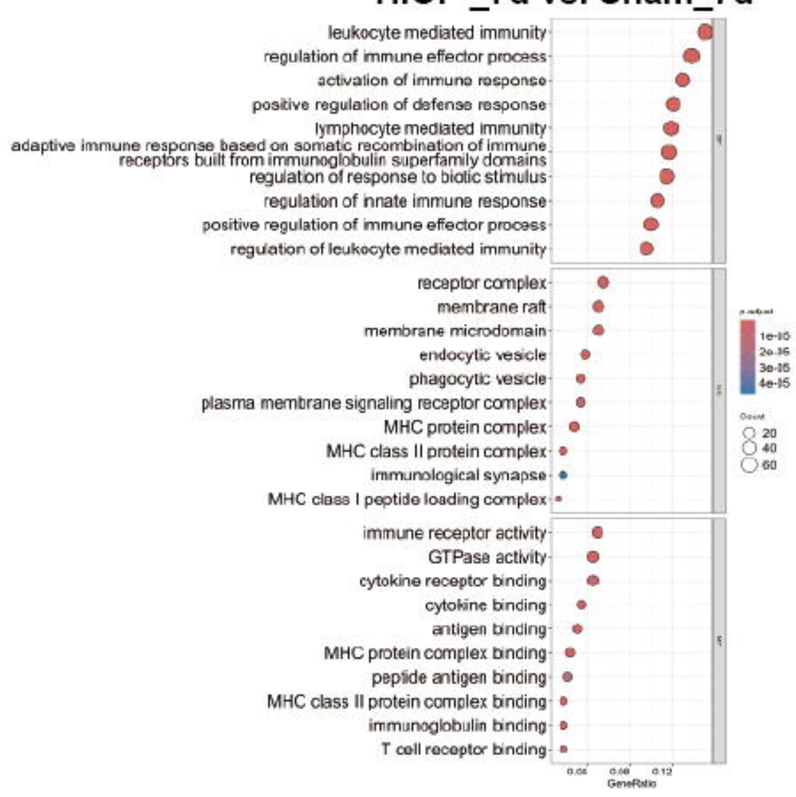

C

Overlapping DEGs
HIOP _7d vs. UPOAO_7d

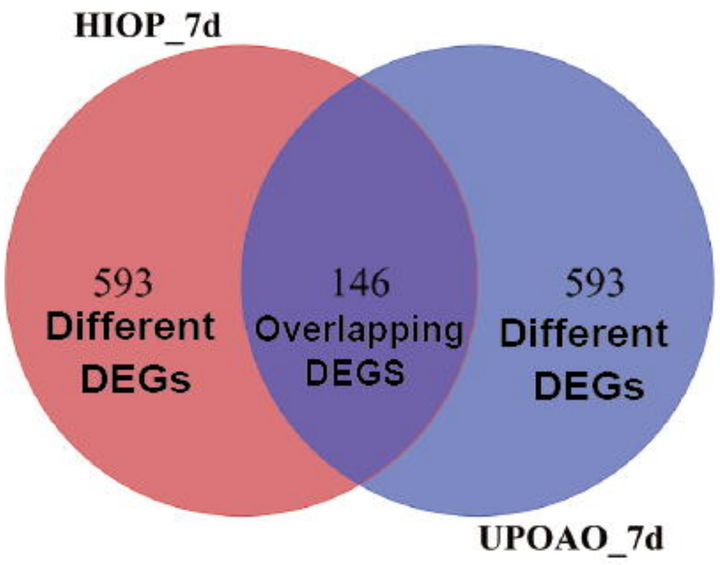

D

GO Erichment
Overlapping DEGs

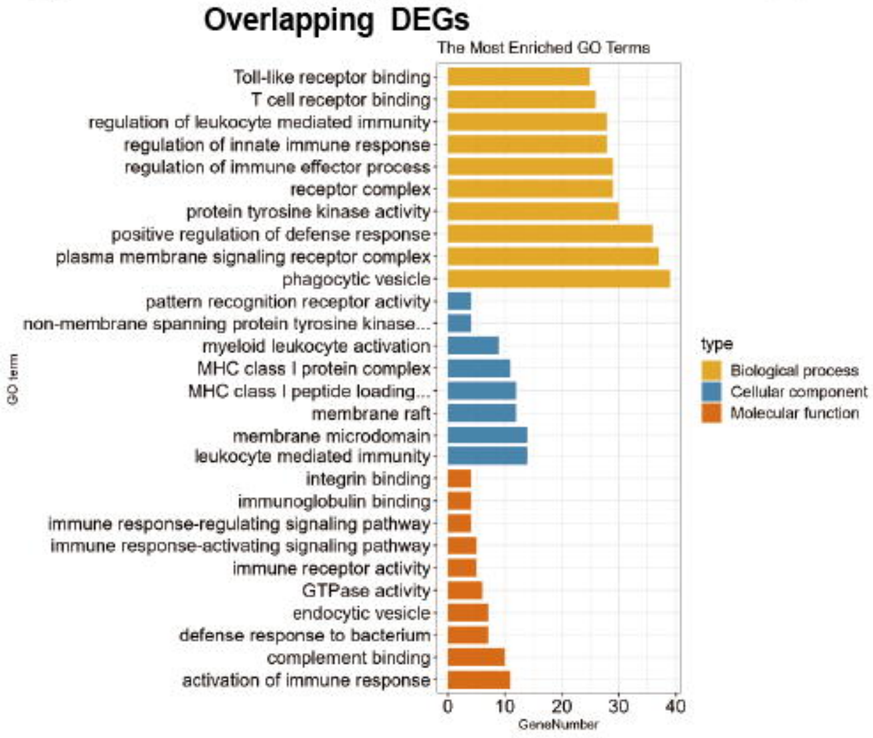

E

GO Erichment
HIOP_7d Different DEGs

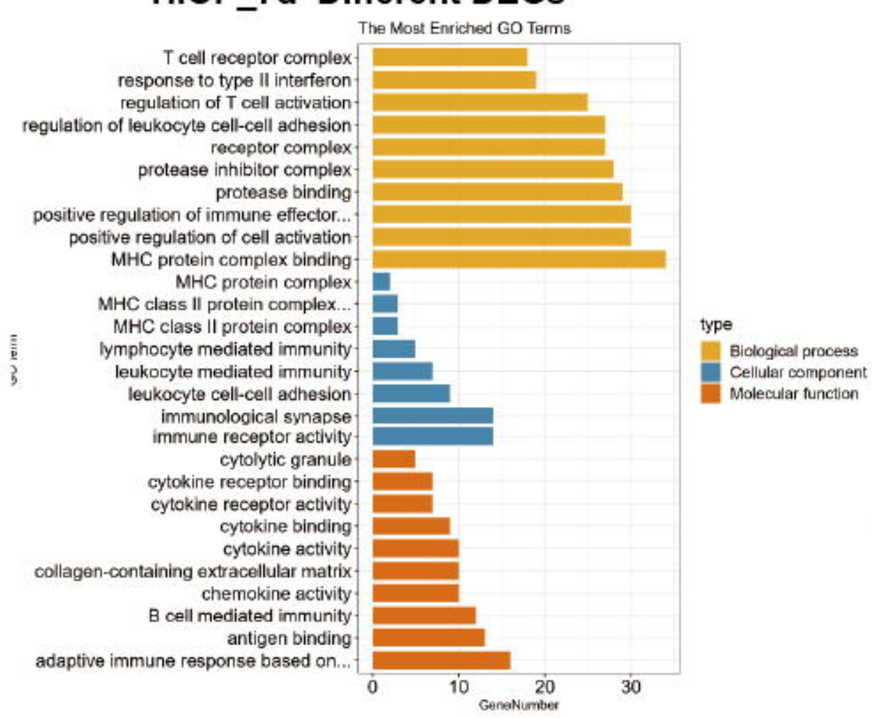

F

GO Erichment
UPOAO_7d Different DEGs

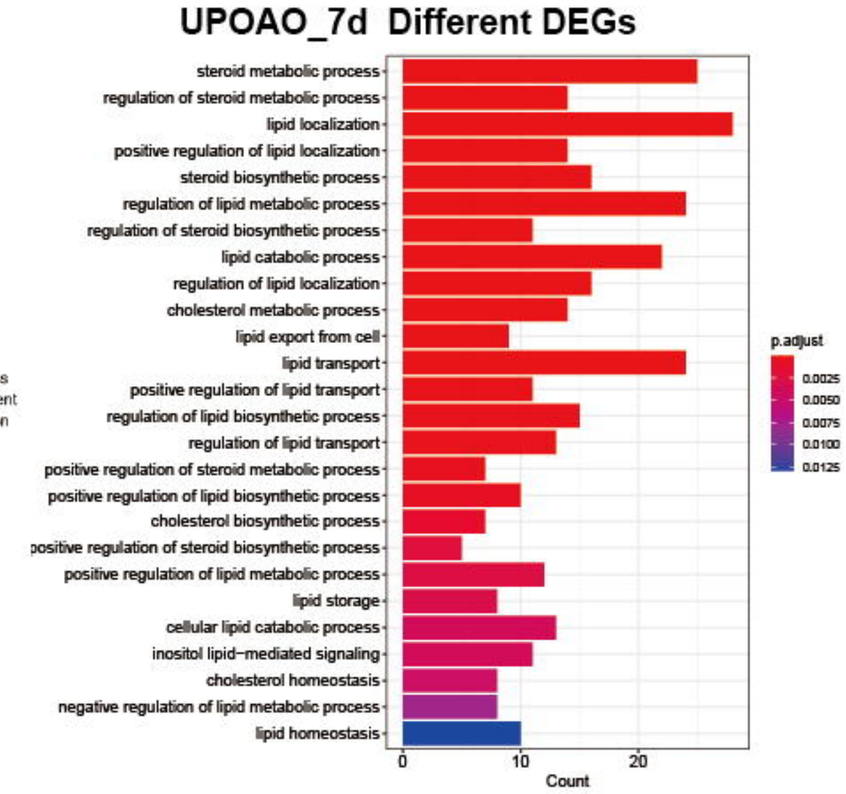

G

Lipid and steroid related DEGs
UPOAO_7d Different DEGs

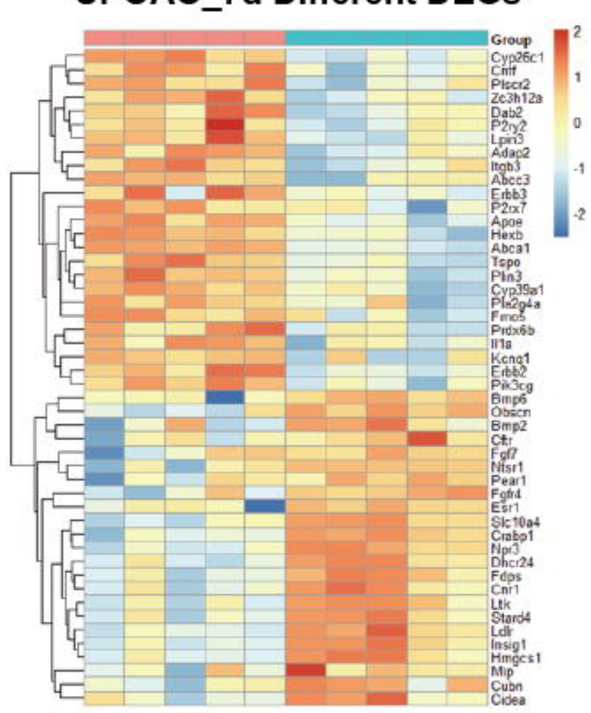

H

UCCAO model

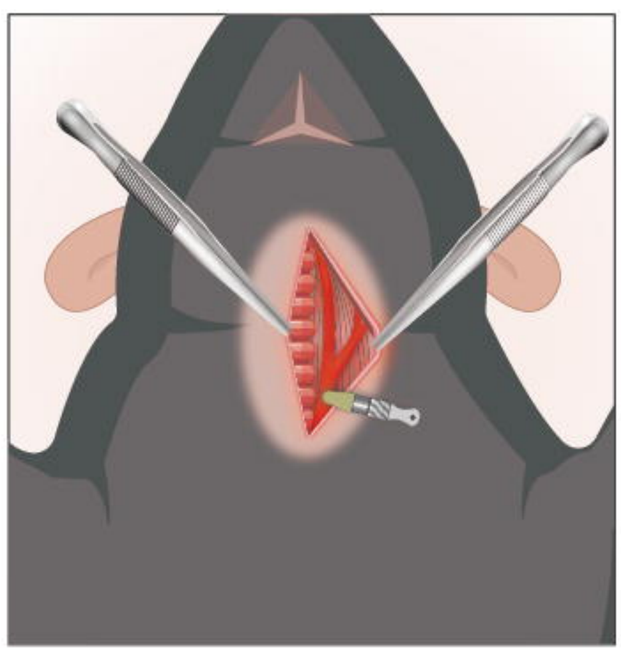

I

DEGs GO Erichment
UCCAO_7d vs. Sham_7d

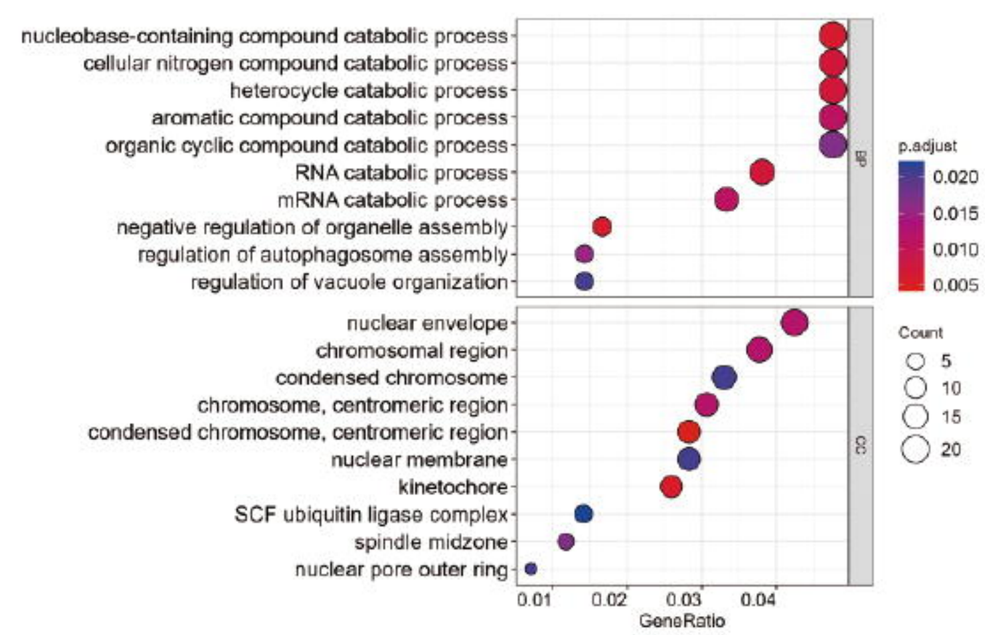

J

PPI Network Analysis
UCCAO_7d DEGs

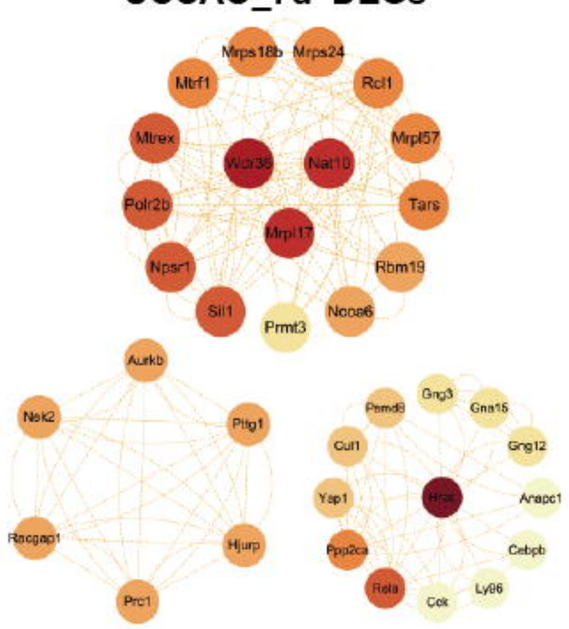

K

Overlapping DEGs
UCCAO_7d vs. UPOAO_7d

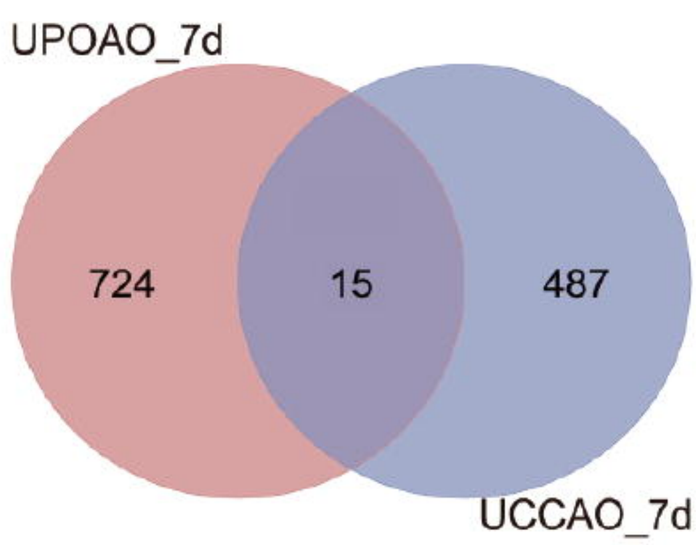

L

Overlapping DEGs
m6A related

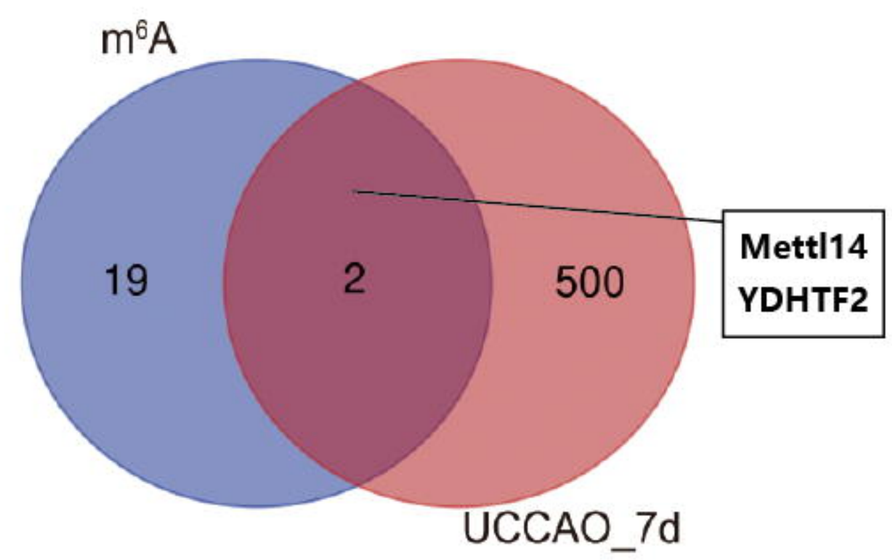

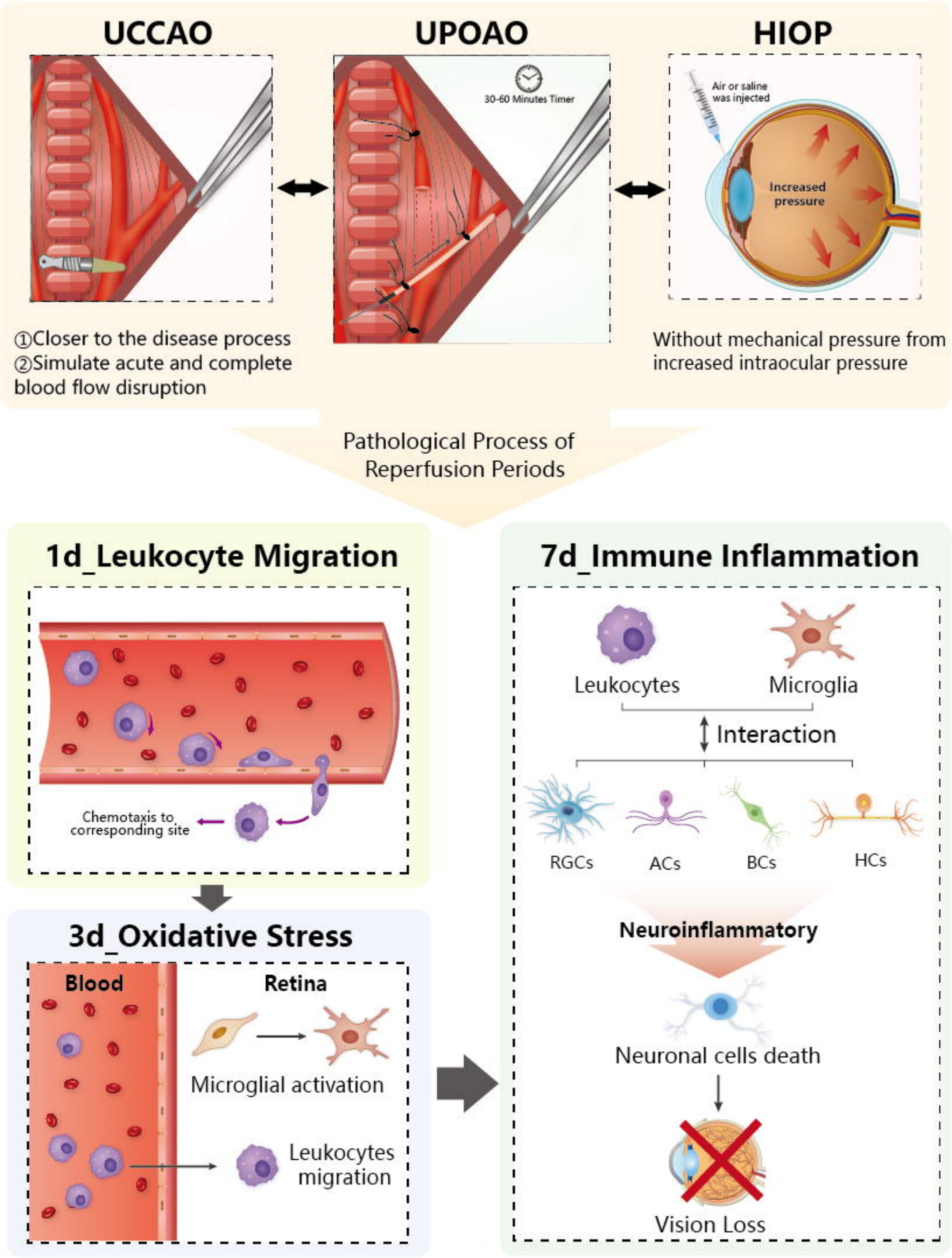
UCCAO
UPOAO
HIOP
30-60 Minutes Timer
Air or saline was injected
Increased pressure
①Closer to the disease process
②Simulate acute and complete blood flow disruption
Without mechanical pressure from increased intraocular pressure
Pathological Process of Reperfusion Periods
1d_Leukocyte Migration
Chemotaxis to corresponding site
3d_Oxidative Stress
Blood
Retina
Microglial activation
Leukocytes migration
7d_Immune Inflammation
Leukocytes
Microglia
Interaction
RGCs
ACs
BCs
HCs
Neuroinflammatory
Neuronal cells death
Vision Loss